Coprecipitation Synthesis of Superplastic 3 Mol. % Yttria – Stabilized Tetragonal Zirconia Polycrystalline / Magnesium Aluminate Spinel Nanocomposite

A Thesis
Presented in Partial Fulfillment of the Requirements for the
Degree of Master of Science
with a
Major in Materials Science & Engineering
in the
College of Graduate Studies
University of Idaho

by
Michael Opoku

January 2015

Major Professor: Raghunath Kanakala, Ph.D.

AUTHORIZATION TO SUBMIT THESIS

This thesis of Michael Opoku, submitted for the degree of Master of Science with a Major in Materials Science & Engineering and titled “Coprecipitation Synthesis of Superplastic 3 Mol. % Yttria - Stabilized Tetragonal Zirconia Polycrystalline / Magnesium Aluminate Spinel Nanocomposite,” has been reviewed in final form. Permission, as indicated by the signatures and dates below, is now granted to submit final copies to the College of Graduate Studies for approval.

Major Professor: ______________________________ Date : ______________
Raghunath Kanakala, Ph.D.

Committee
Members: ______________________________ Date : ______________
Indrajit Charit, Ph.D.

______________________________ Date : ______________
Lee Ostrom , Ph.D.

Department
Administrator: ______________________________ Date : ______________
Eric Aston, Ph.D.

Discipline’s College
Dean ______________________________ Date : ______________
Larry Stauffer, Ph.D.

Final Approval and Acceptance

Dean of the College
of Graduate Studies: ______________________________ Date : ______________
Jie Chen, Ph.D.

ABSTRACT

3 Mol. % Yttria-Stabilized Tetragonal Zirconia Polycrystalline / Magnesium Aluminate Spinel (70%3Y-TZP/30%$MgAl_2O_4$) superplastic nanocomposite have exhibited high strain rate superplasticity at $1.7 \times 10^{-2} - 3.3 \times 10^{-1}\ s^{-1}$. Low strain rate superplasticity ($10^{-5} - 10^{-3}\ s^{-1}$) has been the main drawback of using superplastic ceramics in industries. Microstructural design of 70%3Y-TZP/30%$MgAl_2O_4$ composite is a key in obtaining high strain rate superplasticity within the range of $10^{-2} - 10^{0}\ s^{-1}$. 70%3Y-TZP/30%$MgAl_2O_4$ nanocomposite may experience a surge in its application at high temperature if the microstructure is design to exhibit high strain rates superplasticity at low deformation temperatures.

In the present study, the reverse coprecipitation synthesis technique was adopted to synthesize nanocomposite powders containing 70%3Y-TZP/30%$MgAl_2O_4$ and 60%3Y-TZP/40%$MgAl_2O_4$ with the aim of obtaining microstructural features suitable for exhibiting high strain rate superplasticity at low temperatures. It was anticipated that the coprecipitation synthesis technique route will yield highly homogeneous mixing of the 3Y-TZP phase and the $MgAl_2O_4$ phase at the nano level. Homogeneous mixing of these two phases will ensure effective supply of Al^{3+} and Mg^{2+} ions to the zirconia matrix to accommodate the grain boundary sliding during superplastic deformation. Microstructual features observed after processing powders of 70%3Y-TZP/30%$MgAl_2O_4$ and 60%3Y-TZP/40%$MgAl_2O_4$ revealed that the coprecipitation synthesis is a desirable technique for synthesizing nanocomposite powders for superplastic application.

ACKNOWLEDGEMENTS

This project has been one of the most significant academic challenges I have ever had to confront. Without the support and guidance of my major professor, thesis committee members, family and friends, this project would not have been completed. It is to them I owe my deepest gratitude.

I would wish to express my deepest and sincere gratitude to my advisor, Dr. Raghunath Kanakala, for his excellent guidance, caring abilities, patience, and providing me with excellent atmosphere to conduct research. His wisdom, knowledge and commitment to the highest standard inspired and motivated me. My appreciation goes to my thesis committee members Dr. Indrajit Charit and Dr. Lee Ostrom for their immense contribution in many ways to my research.

I would also like to thank a good friend, Dr. Kerry Allahar, of the Center for Advanced Energy Studies, who through his skill and experienced, trained me on how to use the spark plasma sintering machine and Vickers hardness tester. I also want to thank Duke Debrah Asante and Ebenerzer Jones-Mensah for their advice during the tough times. Finally, I would like to thank my mother, Mavis Serwah for her prayer and encouragement.

DEDICATION

I would like to dedicate this to my mother Mavis Serwah, Sandra Twumwah, Priscilla Preprah , Duke Asante and Ebenerzer Jones-Mensah without whom I could not have done this.

TABLE OF CONTENTS

LIST OF FIGURES

LIST OF TABLES

CHAPTER 1: BACKGROUND INFORMATION

1.1: Superplasticity in Ceramics at High Temperature

The superplastic property of structural ceramics and their composites have attracted considerable attention over the past years, especially in forming and high temperature applications. Superplasticity is defined as the ability of a polycrystalline material to exhibit an exceptionally large elongation (typically over 100% in ceramics and 200% in metallic systems) in tension prior to failure [1-5]. This high temperature deformation mechanism occurs at homologous temperature. Superplasticity has been a common characteristic of fine-grained metals, alloys and intermetallics. In contrast, ceramic superplasticty was discovered about three decades ago. For many years, ceramics were known to be inherently brittle and exhibited no plastic deformation until it was discovered by Wakai in 1986 that yttria-stabilized tetragonal zirconia polycrystal (3Y-TZP) with grain size of 0.3 μm can elongate more than 120% in tension prior to failure at 1450 °C [6]. This unusual elongation of 3Y-TZP ceramic was attributed to a mechanism called grain boundary sliding accommodated by diffusion and dislocation processes [2,7,8]. Uniform occurrence of the grain boundary sliding mechanism coupled with the thermal stability of 3Y-TZP grains at high temperature prevented premature failure during the deformation process. Following Wakai's discovery, research has shown that superplasticity occurs in ceramics with ultrafine grain size of about 1μm or less [9,10]. Strain rates and temperatures at which superplasticity occurs in most ceramics have been reported to be around $10^{-5} - 10^{-3}\ s^{-1}$ and 1400 - 1650 °C, respectively [11,12]. The primary drawback of using superplastic ceramics in industries has been the low strain rates ($10^{-5} - 10^{-3}\ s^{-1}$) exhibited by these materials.

The application of superplastic ceramics in industries requires high strain rate of about $10^{-2} - 10^{0}\ s^{-1}$ [10,13,14]. With current research focusing on designing high strain rates superplastic ceramics, the application of superplastic ceramics may experience a surge in high temperature applications. Complex shaped ceramics will take minutes to be fabricated at low cost and with minimum induced flaws. High strain rates superplastic ceramics can also improve ceramic manufacturing processes such as superplastic forging, extrustion, superplastic joining and deep drawing.

Out of the many superplastic ceramic composites, zirconia-spinel composites have proven to exhibit high strain rate and large elongations at high temperatures [7,11]. Morita et al. [11] had reported a tensile elongation to failure > 300% at strain rates between $1.7 \times 10^{-2} - 3.3 \times 10^{-1} s^{-1}$ in 70% 3Y-TZP/ 30% $MgAl_2O_4$. The 70% 3Y-TZP / 30% $MgAl_2O_4$ composite has been produced solely by a combination of ball milling and spark plasma sintering technique. The results from these techniques have yielded high strain rate superplasticity at low temperatures.

1.2: Microstructural Designs For Achieving High Strain Rate Superplasticity

In general, the strain rate $\dot{\varepsilon}$ of a polycrystalline material is related to the applied stress σ as follows [1,11-13]:

$$\dot{\varepsilon} = A\sigma^{n} \exp(-\frac{Q}{RT})d^{-p} \qquad (1)$$

where A is a constant that represents the frequency of atoms jumping across grain boundary, Q is the activation energy, T is the absolute temperature, R is the gas constant, d is the grain size, p is the grain size exponent and n is the stress exponent.

The n, p, and Q depend on the deformation controlling mechanism. Two observations can be made from Equation (1): Firstly, for a constant applied stress and a constant deformation temperature, the strain rate increases with decreasing grain size. Secondly, the term $A\exp(-\frac{Q}{RT})$ in the equation indicates that enhanced diffusion along the grain boundaries can inhibit grain growth and reduce flow stress thereby increasing the strain rate. One of the approaches for achieving high strain rate superplasticity involves microstructural designs [12,15]. The various microstructural designs that have been used to obtain high strain rate superplasticity in ceramics include:

(a) Grain size reduction - Ceramics with grain size of about 1 μm or less reported to exhibit HSRS can be achieved through nanocrystallization [5,16]. Decreasing the grain size of ceramics increases grain boundaries in the microstructure, which in turn decrease the flow stress and cavity nucleation during deformation [5,9,14]. This results in an increase in strain rate and a reduction in deformation temperature [17]. Grain size reduction also reduces the distance over which atoms diffuse across grain boundaries in order to accommodate the stress concentration in the microstructure [14].

(b) Suppression of dynamic growth - The stabilization of grains in superplastic ceramics at high temperature is a key to obtaining large elongation at high strain rates during high temperature deformation. High temperature deformation of ceramics usually accompanies grain growth and intergranular cavitation in the microstructure [6,9]. During grain growth, the deformation behavior of the material changes due to the increase in flow stress. In the case of intergranular cavitation, small cavities formed during deformation grow into a micrometer-sized holes which eventually interlink to form holes in the microstructure leading to premature failure [2,12,18].

An increase in flow stress and intergranular cavitation during deformation can reduce the tensile ductility and strain rate. Grain growth that occurs during superplastic deformation can be prevented through dispersion of a secondary phase in monolithic ceramic materials [8,11,17,19]. These secondary phases are known to suppress grain growth through Zener pinning mechanism.

(c) Enhanced diffusion - This has been achieved by doping with various cations. Cations of larger sizes and lower valancies are effective in obtaining HSRS [15]. These cations segregate at the grain boundaries and decrease the grain boundary mobility by solute drag effect [20]. In superplastic ceramics, the segregated cations prevent grain growth and decrease the flow stress, thereby increasing the strain rate [15,19]. Effective diffusion is achieved when the cations travel short distance in the microstructure to accommodate grain boundary sliding.

(d) Homogeneous microstructure - Homogeneous microstructure that is devoid of residual pores can also enhance the superplastic property of ceramics. Ceramics with uniform grains size and shapes ensure stress is evenly distributed during deformation [18]. Thus, stress concentration sites and cavity nucleation, which are known to cause premature failures in ceramics are reduced.

1.3: Superplastic Ceramics and Ceramic Composites

Very few ceramics over the years have been shown to exhibit superplasticity at high temperatures. Even monolithic ceramics that possess superplastic ability require a certain amount of doping with some cations or oxides before they can exhibit HSRS and large elongation at low deformation temperatures. This part of the paper gives an overview of the various ceramics and their composites that are known to exhibit superplasticity.

1.3.1: Zirconia Ceramics And Their Composites

Zirconia and its composites are used in various engineering applications such as fuel cells, thermal barrier coatings, cladding materials and other high temperature applications. Pure zirconia however, has limited usage due to the destructive transformation that occurs during tetragonal-to-monoclinic $(t \rightarrow m)$ phase transformation [21,22]. At ambient temperature, the monoclinic phase of zirconia exists, but upon heating, it transforms to the tetragonal phase at 1170 °C [23]. The tetragonal phase is stable up to 2370 °C but transforms to the cubic phase, which remains stable until pure zirconia reaches its melting point at 2683 °C [24]. This phase transformation is reversible upon cooling.

$$\text{Monoclinic(m)} \xleftrightarrow{1170\ ^{\circ}\text{C}} \text{Tetragonal (t)} \xleftrightarrow{2370\ ^{\circ}\text{C}} \text{Cubic (c)} \xleftrightarrow{2683\ ^{\circ}\text{C}} \text{Melt}$$

It is the characteristics of these phases in zirconia that allow it to be used in different applications. Each zirconium atom in the monoclinic phase forms sevenfold co-ordination with oxygen atoms at varying distances. In the tetragonal phase, each zirconium atom is coordinated by eight oxygen atoms which are not equidistant hence leading to the formation of a distorted tetragonal phase [24]. A zirconium atom in the cubic phase, however, is octahedrally coordinated by eight oxygen atoms that are equidistant to each other. The monoclinic phase, is hardly used in high temperature applications due to the high volume expansion associated with the tetragonal-to-monoclinic $(t \rightarrow m)$ phase transformation. This high volume expansion change in tetragonal-to-monoclinic $(t \rightarrow m)$ phase transformation usually leads to crack propagation in zirconia [22,23].

The tetragonal phase exhibits high fracture toughness allowing it to be used in applications such as optical fiber connectors and grinding media [25]. The stabilization of cubic phase with yttria and calcia increases its ionic conductivity due to the creation of oxygen vacancies in the crystal lattice. The high ionic conductivity of the cubic phase allows it to be used in oxygen sensor technology [26].

The driving force of the phase transformation in zirconia is the free energy change. The phase with the lowest free energy is stable at room temperature. Due to the high free energy change of both the tetragonal and the cubic phase compared to the monoclinic phase, it is impossible to stabilize the high temperature phases at room temperature without transforming to monoclinic [23,24]. Yet, research has established that these high temperature phases can be stabilized through nanocrystallization and doping with certain oxides [21,27]. The nanocrystallization method involves maintaining a critical grain size within the microstructure during sintering. Arun et al. [28] reported stabilization of the tetragonal phase of zirconia at room temperature when the grain size was maintained below 15 nm for pure zirconia and 71 nm in zirconia doped with 1.5 moles of yttria, respectively. The second high temperature phase stabilization mechanism involves the use of oxide dopants to stabilize either the tetragonal or cubic or both phases at room temperature. The extent of stabilization of these phases depends on the solubility and concentration of the dopants in zirconia. Swab [24] has described the criteria for selecting oxide dopants for stabilizing the high temperature phases of zirconia and they are as follows:

(1) For an oxide to be selected as a dopant, the ionic radii difference between the zirconium ion and the dopant cation must be small in order to reduce lattice distortion in the crystal lattice which can lead to spontaneous phase transformation.

(2) The dopant cation must have an oxidation state of +2 and +3 in order to produce oxygen vacancies to maintain charge neutrality.

(3) The dopant must have high solubility in Zirconia to ensure microstructural homogeneity.

(4) The crystal structure of the dopant must be cubic or tetragonal depending on the zirconia phase to be stabilized.

Most of the oxides that have been used to stabilize the tetragonal and cubic phase of zirconia are yttria, calcia, magnesia and ceria [23,24,29]. These oxide dopants usually lead to the formation of three types of zirconia: fully stabilized zirconia (FSZ) containing the cubic phase only, partially stabilized zirconia (PSZ) containing a cubic matrix with dispersed tetragonal particles, and the tetragonal zirconia polycrystal (TZP) which contains only the tetragonal phase [24,25]. Depending on the concentration of the oxide dopant, the cubic or the tetragonal phase will stabilize at room temperature. In the case of yttria dopant for example, 3-6% concentration of yttria has been reported to stabilize the tetragonal phase only [30]. Above this concentration the cubic phase is formed. **Figure 1** shows the zirconia-yttria system. The cubic phase is formed at high temperature and high yttria concentration above 7.5% . The monoclinic phase, which is the low temperature phase is formed below the concentration of 2.5%.

In 3Y-TZP, the doping of zirconia with yttria introduces Y^{3+} ion into the ZrO_2 matrix which replace some of the Zr^{4+} ions in the ZrO_2 lattice. The ionic radius of Y^{3+} (1.04 Å) is greater than that of Zr^{4+} (0.86Å); hence Y^{3+} stabilized the tetragonal phase by accommodating the volume expansion that occurs during tetragonal to monoclinic polymorphic transformation. The tetragonal phase of zirconia is attractive for superplastic application compared with monoclinic and cubic phase due to the stabilization of the tegragonal grains at temperatures (1400- 1650 ℃) where most ceramic superplasticity occurs.

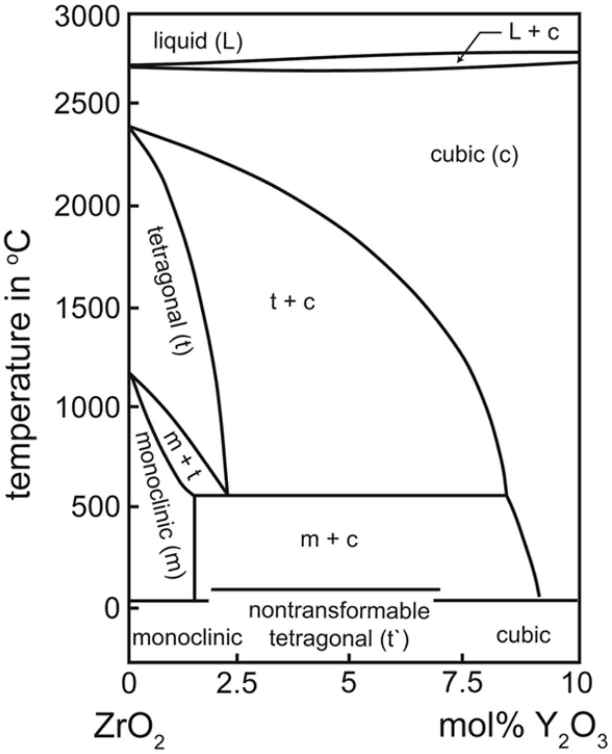

Figure 1: Phase diagram of zirconia-yttria system [adapted from 31]

The 3Y-TZP ceramic has also been doped with different oxides to supply cations in the microstructure during superplastic deformation [14,17,32]. Tohru et al. [31] reported unusual elongation of about 1000% in 3Y-TZP doped with 20% alumina at 1723 K at a strain rate of 1.7×10^{-4} s^{-1} as shown in **Figure 2**. Zirconia and their composites that have exhibited enhanced superplasticity at different strain rates and temperature are shown in **Table 1**. High strain rates superplascity ($10^{-2} - 10^{-1}s^{-1}$) that is of interest to industries has been achieved in zirconia-spinel composites

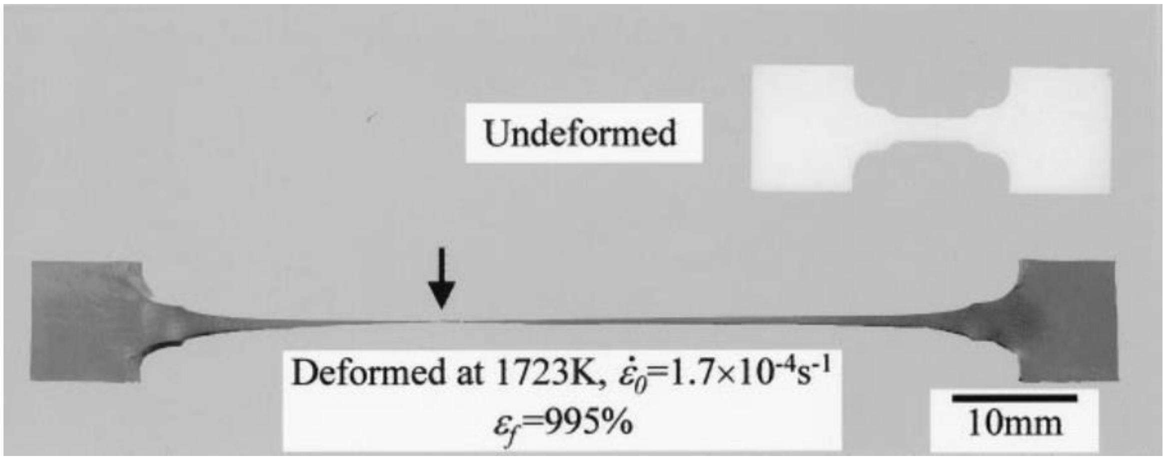

Figure 2: Tensile specimens of 3Y-TZP doped with 0.20 wt% alumina before and after tensile deformation [32].

Table 1 : Zirconia ceramics and their composites with unusual tensile elongation prior to failure.

Material	**Grain Size (µm)**	**Strain Rate (ε^{-1})**	**Elongation e_f (%)**	**Temperature (°C)**	**Ref**
3Y-TZP	0.3	1.1×10^{-4}	>120	1450	[6]
3Y-ZrO_2-30%Spinel	-	1.7×10^{-2}-3.3×10^{-1}	600-300	1525	[18]
40%3Y-ZrO_2-30%Spinel-30%Alumina	0.21	1-0.4×10^{-2}	390- 1040	1650	[7]
ZrO_2-2mol% CaO-2mol%TiO_2	0.25	0.01	360	1400	[21]
ZrO_2-0.2mol%Mn_2O_3-0.3mol % Al_2O_3	0.23	1.2×10^{-2}	600	1450	[33]
ZrO_2-20wt% SiO_2	0.26	1.3×10^{-4}	>1000	1400	[34]

1.3.2: Silicon Nitride Ceramics

Silicon nitride (Si_3N_4) based ceramics has been studied for many years for potential application at high temperatures. Si_3N_4 ceramics are well known for their high flexural strength, high fracture toughness, high temperature strength and excellent creep resistance. These properties make Si_3N_4 attractive for superplastic application. The high temperature superplasticity of Si_3N_4 had been studied in monolithic Si_3N_4 [35,36,37], Si_3N_4/SiC composites [38] and SiAlON [39,40]. A recent report showed that nano-grained Si_3N_4 ceramics containing Y_2O_3-Al_2O_3-MgO glass system as sintering additives deformed in tension to about 302 % of strain rate of 5×10^{-4} s^{-1} as shown in **Figure 3** [35]. β'-SiAlON was also reported to exhibit tensile elongation of 230 % at a strain rate below of 3×10^{-4} s^{-1} [39]. Grain boundary sliding, grain rearrangement along the deformation axis and the presence of viscous flow to accommodate grain rearrangement during deformation are known to be responsible for the enhanced elongation in Si_3N_4 [15,38,41].

The α-Si_3N_4 and β-Si_3N_4 phases of Si_3N_4 have been well studied for superplastic applications. The α-Si_3N_4 is characterized by equiaxed fine grains with high thermal stability at intermediate temperatures. In contrast, the β-Si_3N_4 is characterized by long grains, which grow anisotropically during high temperature deformation [15,42]. Both phases have a high range of solubility. The high solubility of the α-Si_3N_4 and β-Si_3N_4 allow the addition of sintering additives such as Al_2O_3 and Y_2O_3 to enhance densification and facilitate phase transformation [15]. This leads to the formation of α'-SiAlON and β'-SiAlON phases.

The development of superplastic Si_3N_4 is based on two microstructural designs. Densification of SiAlON at low temperature to lower the transformation of α-equiaxed grains to the β-grains [39,42] and the processing of equiaxed grains of β-Si_3N_4 that possess high thermal stability during high temperature deformation [36]. With the introduction of nanocrystallization to designing the microstructure of superplastic Si_3N_4 as shown in **Figure 3**, high strain rates and large elongation will be achieved.

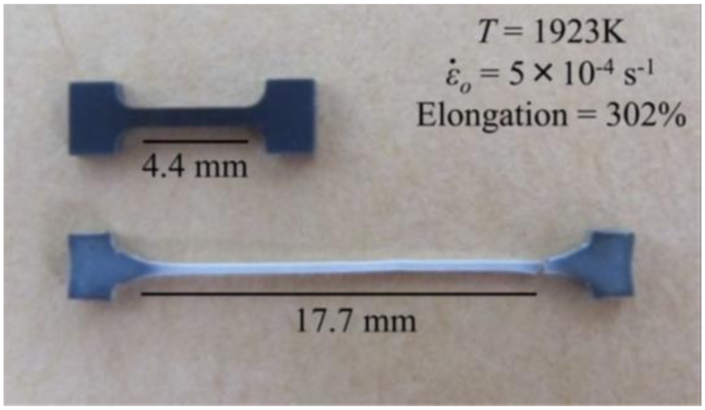

Figure 3: Tensile elongation of Si_3N_4 ceramics at high temperature [35]

1.3.4: Alumina Ceramics

Pure alumina is used in several high temperature applications such as furnace components, coatings, arch lamp tubes, abrasives and thermal insulations. Several attempts to develop superplasticity in pure alumina proved futile due to the rapid grain growth and formation of cavitation during high temperature deformation [43]. For example, the first attempt to develop superplasticity in alumina yielded less than 20% elongation to failure at 1300 °C [44]. This elongation was small compared to those exhibited by zirconia and other superplastic ceramics. Beside the rapid grain growth that occurs in alumina during deformation, alumina also has low solubility for cations which usually result in low cohesive strength of the grain boundaries [15]. In spite of the low solubility of pure alumina, certain oxides have been used as dopants for suppressing grain growth. The maximum elongation obtained from doping pure alumina with MgO was about 70% at 1450 °C [43]. Co-doping pure alumina with TiO_2 and MnO did not only increase the elongation by 100%, but also increase the strain rate [45]. All the above mentioned dopants did not address the issue of grain growth thoroughly. Effective suppressing of grain growth was observed in pure alumina dispersed with spinel particles. Takigawa et al. [46] dispersed 20 % spinel particles in pure alumina which resulted in an enhanced elongation of about 400% at 1550 °C . The spinel particles inhibited grain growth in alumina through pinning effect. Takigawa et al. [46] also observed that, in order to use particles in alumina to suppress grain growth, they must be added in right proportion in order to prevent particle agglomeration which can lower the elongation and the strain rate.

1.3.5: Hydroxyapatite

Hydroxyapatite ($Ca_{10}(PO_4)_6(OH_2)$) (HA) ceramic is well known for its biocompatibility with human bone [47]. Superplasticity in HA has led to the processing of biocompatible products near to net shape with ease. The superplastic property of HA had been shown to depend on the processing parameters. Different processing techniques of HA produced different tensile ductility. Keiichiro et al. [48] used cold isostactic pressing to make a compact HA and then fired the compact from 1000 °C to 1200 °C for 5 hrs. Tensile elongation measured at 1000 °C, 1050 °C and 1110 °C yielded 118%, 156% and 157% respectively. Spark plasma sintering of HA powder at temperatures between 950 °C and 1000 °C improved the tensile elongation to about 270% and 486%, respectively [49].

The key to enhancement in elongation was due to the ability of spark plasma sintering to retain fine grains of HA with pore-free microstructure. In all the above processing techniques, examination of the post deformation microstructure of HA showed that grain boundary sliding was the predominant mechanism during the superplastic flow.

1.3.6: Fe_3C and Fe Ceramics

Superplasticity has been observed in ceramic based material containing 80 Vol% of fine grained iron carbide matrix and 20 Vol% of iron serving as a second phase. Powders of the two mixtures were compacted and extruded at 1050 ℃. Elongations between 370% - 610% were obtained at different strain rates of 2×10^{-4} and $1 \times 10^{-4}\ s^{-1}$, respectively [50]. Both experiments were performed at high temperature of about 1035 ℃. The iron phase was introduced into the Fe_3C matrix to inhibit grain growth at high temperature. The average grain size of the extruded composite before and after tensile deformation was between 2-4 µm [50]. Kim et al. [50] reported that strain rate sensitivity was not the only criterion for achieving high strain rate in Fe_3C and Fe composite but also the incorporation of a second phase in Fe_3C matrix to suppress grain growth.

1.4: Nanocomposites Synthesis Techniques

Nanocomposites encompass two or more materials of different properties with one-dimensional to three - dimensional distribution of individual phases mixed at the nano level. [51,52]. Nanocomposite materials combine properties of individual constituents to produce performance characteristics far greater than that of a monolithic component [51,53].

In engineering application, nanocomposites are produced in a form of powders, thin films or dense components depending on the application. The structure of nanocomposite is compose of atomic structure, composition, microstructure, defects and interfaces.

These structural compositions are controlled by thermodynamics and kinetics of the synthesis and processing techniques [54]. The synthesis techniques for processing nanocomposites falls under three main categories. They are the solid state synthesis, liquid or chemical synthesis and vapor state synthesis. Each synthesis technique has advantages and disadvantages. The choice of a synthesis technique for producing nanocomposites depends on the desired properties and application. This section explores the above menstioned techniques for producing nanocomposites.

1.4.1: Solid State Synthesis of Nanocomposites

Solid state synthesis involves the use of mechanical energy to cause deformation under shear condition, leading to formation of nanostructured particles of different sizes and shapes [54]. The deformation also introduces defects such as vacancies, dislocations, grain boundaries that enhance atomic diffusion in the microstructure.

Mechanical alloying (MA) and mechanochemical synthesis are the two main techniques under solid state synthesis. The MA synthesis techniques uses high energy ball milling to mix different powder particle in order to achieve the desired microstructure of the composite. This technique involves cold welding, fracturing and a subsequent rewelding of powder particles in high-energy ball mill [55,56]. As shown in **Figure 4**, the synthesized powder particles are trapped between two colliding surfaces of the milling media. The collosions between the surfaces causes a reduction in the initial size of the particles. This technique allows the synthesis of different nanocomposite material such as metal-metal, metal-ceramic, metal-nonmetal [57,58]. Disadvantages of the MA process include the contamination of powders by milling medium and the lack of control of particle size [56,58].

Examples of nanocomposites synthesized by the MA technique include Al-Al_2O_3, MoSi-Si_3N_4 [53], Zn/Al_2O_3 [59], and 70%3YTZP/30% $MgAl_2O_4$ [3,11].

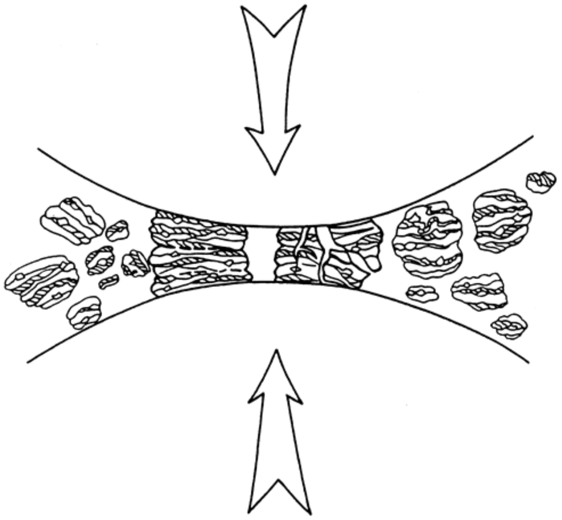

Figure 4 : Schematic illustration of powder particles trapped between two colliding surfaces [57].

1.4.2. Chemical Synthesis of Nanocomposites

Chemical synthesis techniques are well known for simplicity and the ability to control particle shapes and sizes during the synthesis process [60]. These techniques involve chemical reactions between two or more precursors in solution. The precursor precipitates from solution when super saturation is reached. Chemical synthesis technique has advantage over solid state synthesis due to the ability of atoms to diffuse easily resulting in homogenous mixing of components [54]. The various synthesis techniques under this category are the chemical coprecipitation, sol-gel and hydrothermal synthesis techniques.

1.4.2.1: Chemical Coprecipitation

Coprecipitation synthesis technique involves precipitating two or more metal hydroxide in a form of a gel from a precursor metal salt solution [54,61,62].

Inorganic metal salt of nitrate, chloride, acetate or oxychloride are used as precursors because of their high solubility in water and their ability to produce metal ion in solution [60]. These salts are dissolve in water and the solution formed is stirred continuously to increase the motion of ions and also decrease localized buildup of concentration of ions by keeping the solution thoroughly mixed. The pH of the resulting solution is increased by introducing the solution in a basic solution. This step is very important in the synthesis process because the final particle size is determine at this stage. Increasing the pH of the solution increases the concentration of OH^- in solution. The metal ions from the precursor solution react with the OH^- to form hydroxide particles. The excess OH^- in solution adsorb on the formed particle surfaces, thereby creating some form of electro repulsion among particles formed in solution [54]. This electro repulsion prevents aggregation of the as-synthesized particles. This causes a reduction in the particle size [63]. The precipitates formed are then washed with water to remove traces of chloride and nitrate ions from the precursor. Residual ions such as chloride ions that adsorbed on particle surfaces have been found to impede particle sintering [64]. Hence, removal of chloride ions from the particle surface enhance particle sintering. Particle agglomeration is the main drawback of this synthesis technique [60]. An agglomeration of particles is reduced when the precipitates are washed with organic solvents. The washing of powders with organic solvent prevents hydroxyl chemical bridges formation between adjacent particles [61,65,66]. The surface of the powder is then replaced with low surface tension of organic solvent compounds which evaporates during calcination. The hydroxide gel are then centrifuged and dried. The dried powder is calcined to obtain the desired crystalline phase. The ability to control particle size in this synthesis technique makes it possible to synthesize nanocomposites of different sizes and shapes [63]. The coprecipitation method of synthesizing nanocomposites is also very simple and economical compared to other synthesis techniques. **Figure 5** shows the step by step coprecipition synthesis technique.

Figure 5 : Schematic of the steps in the coprecipitation synthesis technique

1.4.3: Vapor Phase Synthesis Technique

In the vapor synthesis route atoms and molecules from precursors are generated in vapor form followed by a condensation process to form nanoparticles [60,69]. The vapor may be generated by thermal and laser beam sources. The size and shape of the particles formed through this technique depends on the condensation time, precursor composition, temperature and pressure of the vapor formed. The inert gas condensation technique falls under this category.

1.4.3.1: Inert Gas Condensation

The inert gas condensation (IGC) technique involves evaporating a metallic source in an inert gas environment followed by cooling to form nanoparticles [69,70]. A typical IGC set up as shown in **Figure 6** consist of a glass cylinder, heating element , crucible to contain the material to be synthesized and a particle collector which rotates during the process to in order to obtain a homogenous mixture [60,71]. During the process, the material to be synthesized is heated by the heating element to form a vapor in a chamber under vacuum condition. The chamber is refilled with inert gas to a low pressure. As the metal vapor rises, it collides with the inert gas atoms and cools during the process. The particles become supersaturated and then nucleate homogeneously during the process [60]. The formed particles are collected by the water cool particle collector. The particles are then scrap off the collector and compacted to produce the nanocomposite. Examples of nanocomposites produce by this method include silver/iron oxide [71]. The IGC synthesis technique is very expensive especially when used to synthesize ceramics with high melting temperatures. One advantange of this technique is that particle size and shape can be controlled by modifying the condensation process [60].

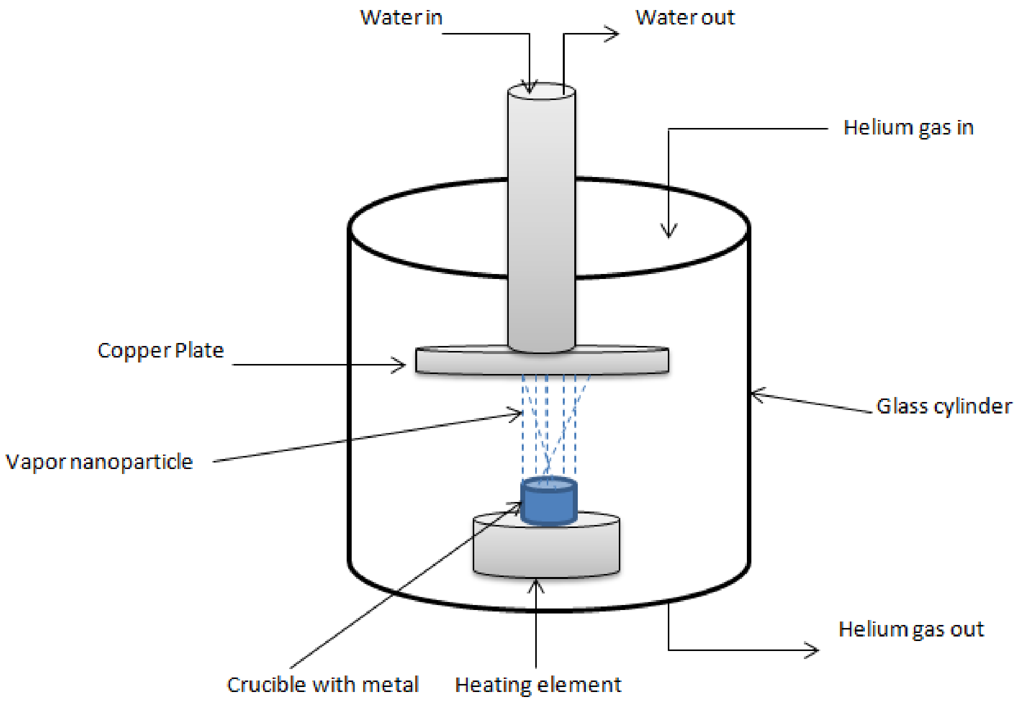

Figure 6 : Schematic of the IGC set up [60]

1.5: Research Objectives

In the present study, the reverse coprecipitation synthesis technique was adopted to synthesize nanocomposite powders containing 70%3Y-TZP/30%$MgAl_2O_4$ and 60%3Y-TZP/40%$MgAl_2O_4$ with the aim of obtaining microstructural characteristics suitable for exhibiting superplasticity. It was anticipated that the coprecipitation synthesis technique route will yield highly homogeneous mixing of the 3Y-TZP phase and the $MgAl_2O_4$ phase at the nano level. Homogeneous mixing of these two phases will ensure effective supply of Al^{3+} and Mg^{2+} ions to the zirconia matrix to accommodate the grain boundary sliding during superplastic deformation. An understanding of the microstructural evolution during the reverse coprecipitation process is essential in obtaining dense nanocomposite ceramic for superplastic application. The emphasis of this research was placed on obtaining uniform mixing of the powders in the hydroxide state in order to obtain homogenous mixing of the 3Y-TZP and $MgAl_2O_4$ phases.

Microstructural characterization of the powders was performed using the X-ray diffraction (XRD), scanning electron microscopy and transmission electron microscopy . The powders obtained through the reverse coprecipitation were sintered using the spark plasma sintering equipment at different sintering temperatures and sintering dwell times. Characterization of the density and hardness was performed to understand the effect of sintering on mechanical properties.

CHAPTER 2: EXPERIMENTAL PROCEDURE

2.1: Synthesis of 3Y-TZP/$MgAl_2O_4$ Powders

Nanocomposite powders containing 3 mol % Yttria-Stabilized Tetragonal Zirconia Polycrystalline / Magnesium Aluminate Spinel (3Y-TZP/$MgAl_2O_4$) were synthesized by the reverse coprecipitation synthesis technique. The compositions of the powders were 70%3Y-TZP/30%$MgAl_2O_4$ and 60%3Y-TZP/40%$MgAl_2O_4$. The reactants for the synthesis of 3Y-TZP/$MgAl_2O_4$ nanocomposite powders were $ZrOCl_2.8H_2O$ (98%, Alfa Aesar, Heysham, England), $Y(NO_3)_3.6H_2O$, (99.9%, Alfa Aesar, Ward Hill, MA), $Mg(NO_3)_2.6H_2O$, (98 %, Alfa Aesar, Ward Hill, MA), $Al (NO_3)_3.9H_2O$, (98%, Alfa Aesar, Ward Hill, MA) and NH_4OH, (28 wt. % Alfa Aesar, Ward Hill, MA) and $(CH_3)_2CHOH$, (99 +% Alfa Aesar, Ward Hill, MA). A detailed schematic of the synthesis route is presented in **Figure 7**. The initial step of the synthesis process involves dissolving a 3.954 g of $ZrOCl_2.8H_2O$ and 0.1454 g of $Y(NO_3)_3.6H_2O$ in 40 ml and 10 ml of deionized water respectively. The two solutions were mixed together after the dissolution of the two salts. The measured pH of the combined solution was around 1.24. The mixed solution was then introduced in drop wise into a vigorously stirred 200 ml of NH_4OH solution with an initial pH of 13.2. The solution was continuously stirred for 20 minutes during which metal hydroxide precipitated from solution. The final pH of the precipitated solution was kept above 12 at all time during the synthesis process. Separately, 0.724 g of $Mg (NO_3)_2.6H_2O$, and 2.118 g of $Al (NO_3)_3.9H_2O$ were dissolved in 10 ml of deionized water respectively and then mixed together afterwards. The measured pH of the resulting solution was 2.53. The solution was subsequently introduced in drops into a 200 ml of NH_4OH solution to form a metal hydroxide precipitate. The two metal hydroxide precipitates of 3Y-TZP and $MgAl_2O_4$

solutions were carefully mixed together and stirred for another 20 minutes until there was a homogeneous mixing of the two solutions. The hydroxide mixture was then centrifuged and washed five times with deionized water followed by a wash with 200 ml of $(CH_3)_2CHOH$. The washing of the powder with $(CH_3)_2CHOH$ is a crucial step in the synthesis process. This is because washing of the powders with $(CH_3)_2CHOH$ reduces the extent of particle agglomeration. The wet precipitates were then dried for two days in air. After drying, the soft agglomerated powders were crushed in a mortar and pestle to form a fine powder. The as-synthezied powders were then calcined at 1000 ℃ for 2 hours to transform the metal hydroxides to oxides.

Characterization of the calcined powders and the sintered samples were carried out by X-ray diffraction (XRD) on a (Brucker D8 advance, Madison, WI). The X-ray diffraction patterns were recorded in the range of $20^{\circ} \leq 2\theta \leq 80^{\circ}$ with step of 0.10 °. For the powder characterization, samples were prepared by grinding the calcined powders using mortar and pestle. The ground powders were smeared uniformly onto a glass slide and mixed with isopropanol to prevent powder particles from falling. The flat surface glass slide was allowed to dry and then loaded into the sample holder for the X-ray diffraction analysis. The experiment was run using Cu-Kα radiation. For the sintered samples, each of the samples were prepared by grinding and polishing with silicon carbide abrasives to a final grit of about 1200 microns.

Scanning electron microscopy (SEM) (JOEL JSM-6610LV,USA) was performed on both the calcined powders and the sintered specimen. The calcined powders were smeared uniformly onto a silicon wafer and loaded into the SEM chamber. Images showing the extent of particle agglomeration were obtained from the SEM. The sintered samples were prepared by grinding and polishing with silicon carbide abrasives and diamond suspensions to a final grit size of 0.5µm.

The morphology of the 70% 3Y-TZP/30% $MgAl_2O_4$ calcined powder was examined by transmission electron microscopy (TEM: Model Tecnai TF30 – FEG STwin STEM, Hillsboro, USA). The sample for the TEM analysis was prepared by dispersing calcined powders in isopropyl alcohol followed by grinding. A drop of the well dispersed powder suspension was deposited on a carbon coated copper grid. Digital TEM images and STEM line scan were taken for analysis.

Sintered samples were produced in a spark plasma sintering machine (Dr. Sinter Lab SPS, 515S SPS, Syntax Inc., Kanayawa, Japan). Each sintered sample was prepared by using 3.00 g of 3Y-TZ/$MgAl_2O_4$ powder. The powder was poured into a conducting die of inner diameter of 12.7 mm and height of 30 mm. The sintering conditions were as follows: 9 kN load equivalent to 71 MPa, heating rate of 100 °C/ min, sintering temperature was between 1200 °C −1300 °C and sintering dwell time ranges from 0 to 20 minutes. The densities of the sintered samples were measured using the Archimedes principle and compared with the theoretical densities.

The Vickers hardness (Leco Micro hardness Tester LM 247AT) of the sintered samples was recorded using a diamond indenter. Samples were mounted and polished using silicon carbide to a final grit of 1200 microns. Each Vickers hardness test was executed using a load of 1k gf at 15 seconds dwell time. Six measurements were recorded for each sample with 200 µm spacing between indent. The Vickers hardness values were computed according to the following equation [72].

$$HV = 1.8544 \times \frac{P_1}{d_1^2} \qquad (2.1)$$

Where P_1 is the force in, kgf and d_1 is the mean diagonal length of the indentations in, mm. The reported hardness values were the averages of all the six measurements taken for each sample.

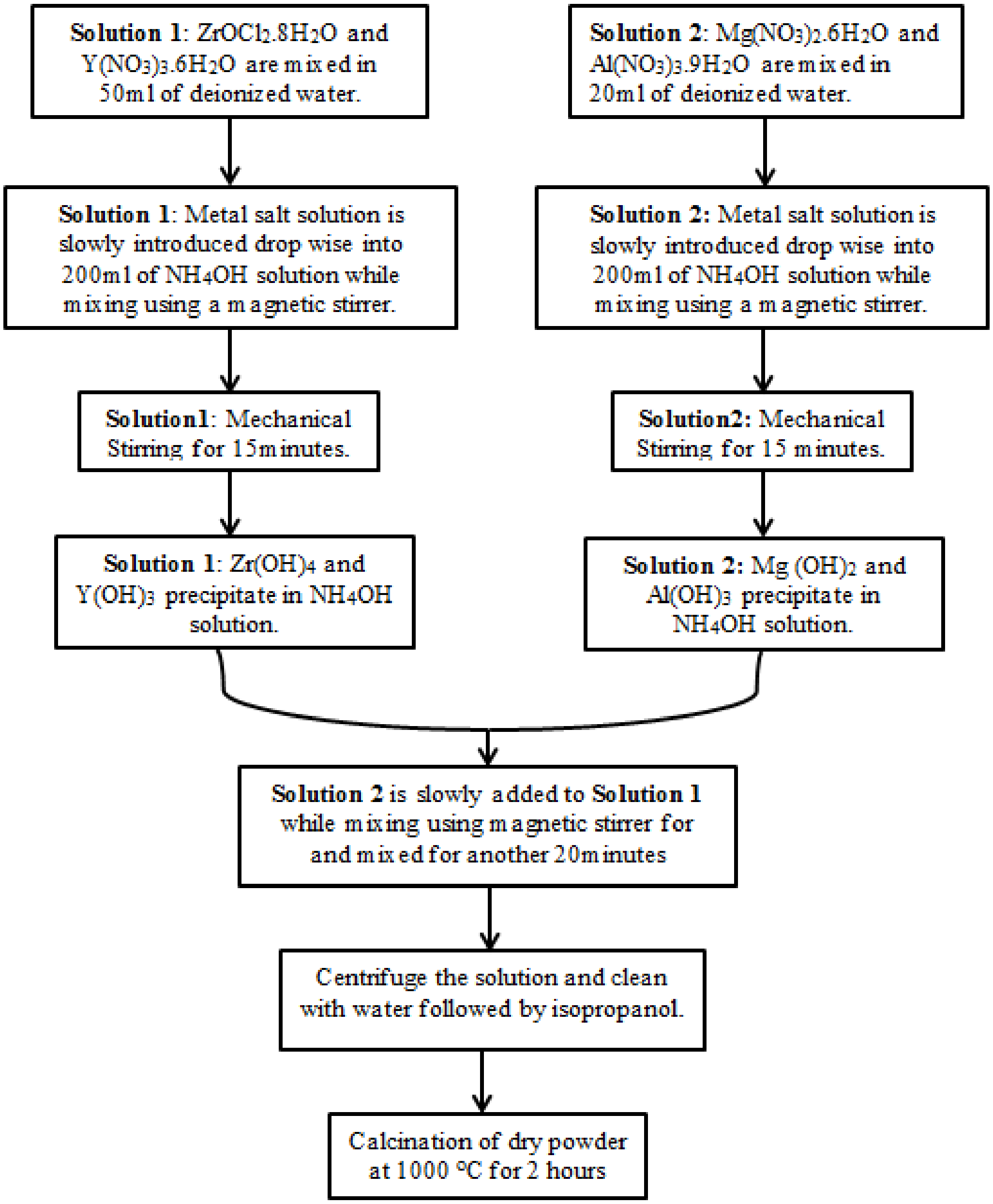

Figure 7 : Flow diagram for processing 3Y-TZP/$MgAl_2O_4$ powder by coprecipitation route

CHAPTER 3: RESULTS AND DISCUSSION

3.1: Synthesis and Characterization of 3Y-TZP/$MgAl_2O_4$ Powders

Figure 8 shows the SEM images of the 70%3Y-TZP/30%$MgAl_2O_4$ and 60%3Y-TZP/40%$MgAl_2O_4$ calcined powders. The SEM images illustrate different particle sizes ranging from small to large particle agglomerates. The particle agglomerates were soft and easily broken down into fine particles. Nanoparticles often cluster to form agglomerates due to their large surface area and high surface energy [54]. Washing of powders with organic solvents in the coprecipitation synthesis process prevents chemical bridge formation between adjacent particles through hydroxyl group present on the particles surfaces [61,65,66]. These hydroxyl groups are replaced by isopropoxy groups from the isopropanol, which will evaporate upon heating. The soft agglomerates of the 3Y-TZP/$MgAl_2O_4$ calcined powders were due to the wash with isopropanol.

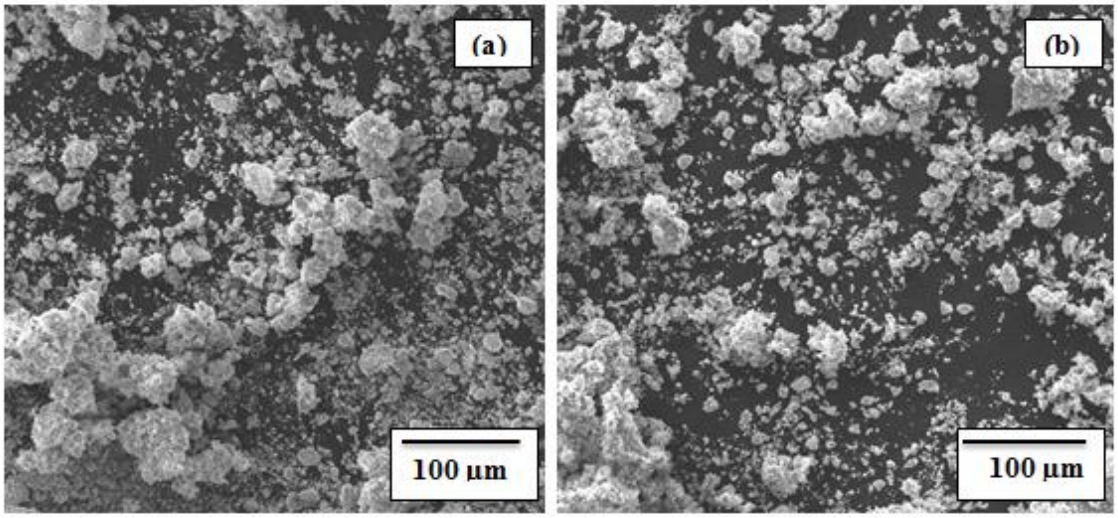

Figure 8 : Scanning electron microscope images of (a) 70%3Y-TZP/30% $MgAl_2O_4$ (b) 60% 3Y-TZP/40% $MgAl_2O_4$ powders calcined at 1000 °C.

Figure 9 shows the X-ray diffraction patterns the 70%3Y-TZP/30%$MgAl_2O_4$ and 60%3Y-TZP/40%$MgAl_2O_4$ nanocomposite calcined powders. The phase analysis of the diffraction patterns show that both the tetragonal zirconia and spinel phases were present. There was no cubic phase of zirconia formed. The patterns could be completely indexed to the standard diffraction pattern (pdf card number - 01-089-9068) of tetragonal unit of yttria-stabilized zirconia belonging to P42/nmx space group and the standard diffraction pattern (pdf card number -00-003-0901) of the cubic unit of spinel belonging to the Fd-3m space group. The phase analysis clearly demonstrates that no ternary phase was formed.

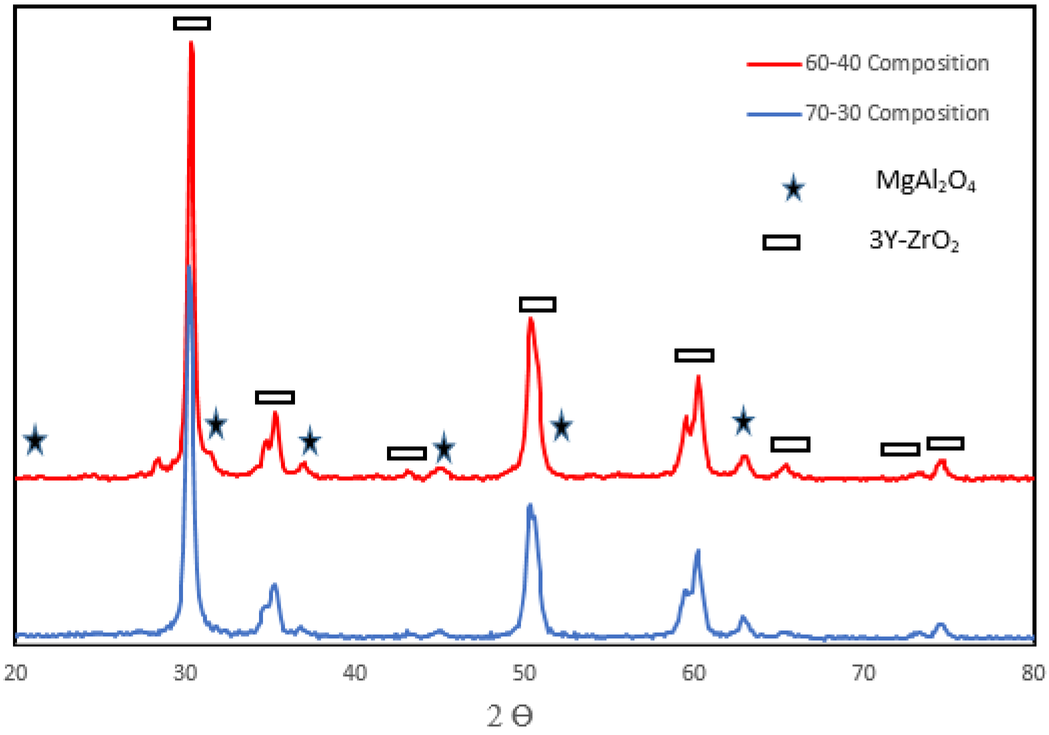

Figure 9 : X-ray diffraction patterns of the 70%3Y-TZP/30% $MgAl_2O_4$ and 60% 3Y-TZP/40%$MgAl_2O_3$ nanocomposite powders calcined at 1000 °C

3.1.1: Crystallite Size Calculation / Estimation

From the Xray diffraction patterns in **Figure 9**, the average crystallite size of the intense peaks were calculated for both 70% 3Y-TZP/ 30% $MgAl_2O_4$ and 60% 3Y-TZP/40% $MgAl_2O_4$ using the Debye-Scherer equation [73].

$$D(\text{nm}) = \frac{0.9}{\cos} \tag{3.1}$$

Where λ is the wavelength of X-ray (0.1541nm), β is the FWHM (full width at half maximum), θ is the diffraction angle and D is crystallite size. **Table 2** and **Table 3** show the measured FWHM values and the corresponding crystallite size for 70% 3Y-TZP/ 30% $MgAl_2O_4$ and 60% 3Y-TZP/40% $MgAl_2O_4$.

Table 2 : The FWHM values and the corresponding crystallite size of the 70% 3Y-TZP/30% $MgAl_2O_4$ calined powder.

2θ of intense peak (degree)	FWHM (degree)	Crystallite size (nm)
30.26389	0.46423	17.7
35.04701	0.92207	9.0
36.73658	0.29345	28.5
43.20941	0.46848	18.2
44.94884	0.61472	13.9
50.47403	0.80768	10.9
60.04405	0.89222	10.3
62.95574	0.5183	18
65.29823	0.39661	23.8
73.13153	0.58268	17.0
74.57965	0.57357	17.4

Table 3 : The FWHM values and the corresponding crystallite size of the 60% 3Y-TZP/ 40% $MgAl_2O_4$ calcined powder

2*θ* of the intense peak (degree)	**FWHM (degree)**	**Crystallite size (nm)**
28.36792	0.43802	18.7
H30.33537	0.41286	19.9
35.20285	0.65112	12.8
36.97076	0.48844	17.1
43.1104	0.52445	16.3
44.96611	0.97142	8.8
50.5156	0.77848	11.3
60.09506	0.87323	10.5
62.96671	0.51481	18.1
65.37099	0.5697	16.6
73.39742	0.29766	33.3
74.59023	0.63029	15.8

The average crystallite size calculated for 70%3Y-TZP/30%$MgAl_2O_4$ and 60%3Y-TZP/40%$MgAl_2O_4$ compositions were 16.8 nm and 16.6 nm respectively. The formation of nanoparticles by the coprecipitation synthesis route is strongly dependent on the pH of the precipitating solutions [63]. High pH provides an excess OH^- concentration in the solutions that adsorb on the particle surface as a hydroxide layer preventing adjacent particles from approaching other particles [54,73]. This causes a decrease in particle size.

Figure 10 shows the TEM image and particle size distribution of the 70%3Y-TZP/30% $MgAl_2O_4$ calcined powder. The TEM micrograph reveals agglomerated powder containing primary particles. The agglomerations as indicated were soft and easily broken into finer powder particles. The image also shows that the particles have a range of distribution. Smaller particles attached onto larger particles. As a whole, it is visible that the powder contains nanoparticles. The average particle size was estimated using ImageJ 1.48 bundled with 64–bit Java. An average particle size of 16nm was recorded. This is consistent with the crystallite size estimation from the Xray diffraction pattern. The analysis illustrates that an average particle is made of one crystallite.

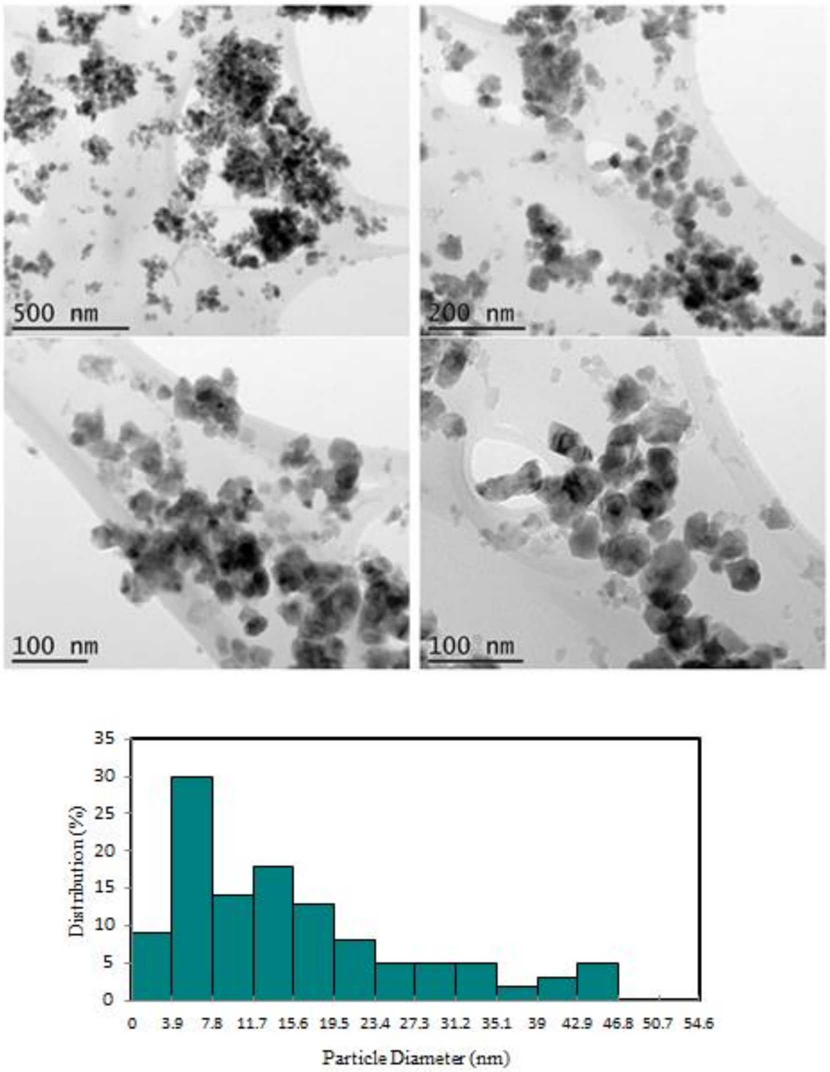

Figure 10 : TEM images at different magnification and particle size distribution of the 70%3Y-TZP/30%$MgAl_2O_4$ calcined powder.

Figure 11 shows a STEM line scan of the 70 %3Y-TZP/30%$MgAl_2O_4$ calcined powder. The line scan shows elemental composition of the nanocomposite. The line scan also shows two phases are coexistant at the nano level. This gives an indication of a true composite containing two phases without any ternary phase formations.

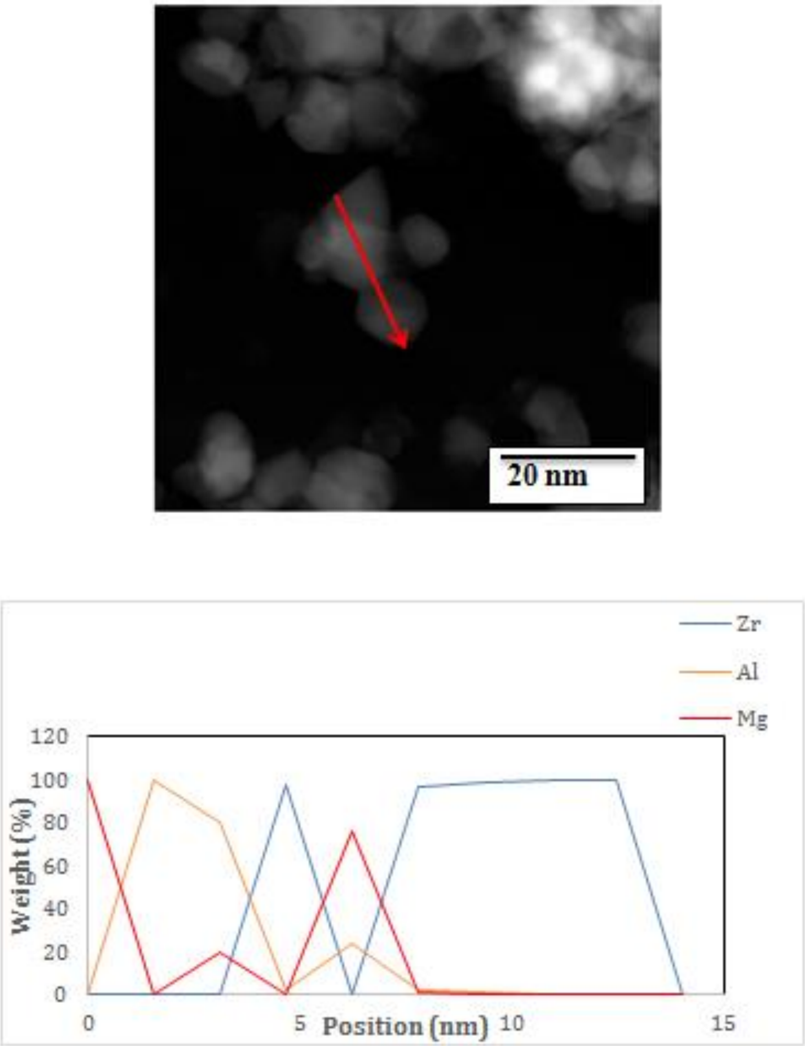

Figure 11 : Shows a STEM line scan of the 70%3Y-TZP/30%$MgAl_2O_4$ calcined powder

Figure 12 illustrates a HRTEM image of a single particle of the 70% 3Y-TZP/30%$MgAl_2O_4$ calcine powder. The HRTEM image shows interplanar distances of 0.295 nm of the 999 peak intensity of 3Y-TZP corresponding to the (101) plane and 0.244 nm of 100 intensity of $MgAl_2O_4$ corresponding to the (311) plane. These results demonstrate that the 3Y-TZP and $MgAl_2O_4$ phases are in close proximity, hence are homogeneously mixed at the nano level. The close proximity of the two phases gives indication that, the $MgAl_2O_4$ phase will effectively supply Mg^{2+} and Al^{3+} cations to the 3Y-TZP matrix to enhace the accommodation process during grain boundary slidding. Also, the Mg^{2+} and Al^{3+} cations can prevent grain growth by grain boundary pinning and thereby reducing the flow stress.

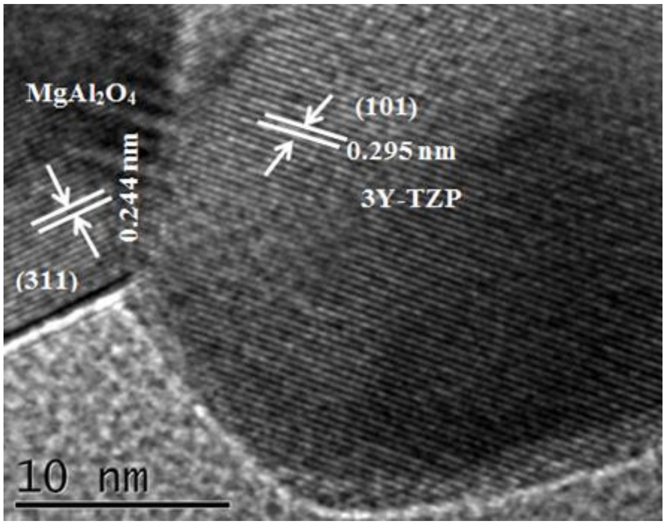

Figure 12 : HRTEM of a single particle of the 70% 3Y-TZP/30%$MgAl_2O_4$ calcined powder

3.2 : SEM image of Sintered Microstructure

Figure 13 shows the SEM images of the 70% 3Y-TZP/30%$MgAl_2O_4$ and 60% 3Y-TZP/40%$MgAl_2O_4$ sintered sample. The microstructure of the two compositions look almost the same. The dark and white contrasts represent the spinel grain and the zirconia grain respectively. The contrasts between the two phases was due to the magnetic stirring mechanism used during the coprecipitation synthesis process. The SEM images of the sintered samples show that both the spinel and tetragonal zirconia phases are homogeneously mixed. Due to invisible grain boundaries of the zirconia grains only the spinel grains were analyzed. The grain size of the spinel was analyzed using ImageJ 1.48 bundled with 64 - bit Java for the 70%3Y-TZP/30%$MgAl_2O_4$ sintered sample. An average grain size 27 nm was recorded. The result indicates there was a slight increase in grain size after sintering.

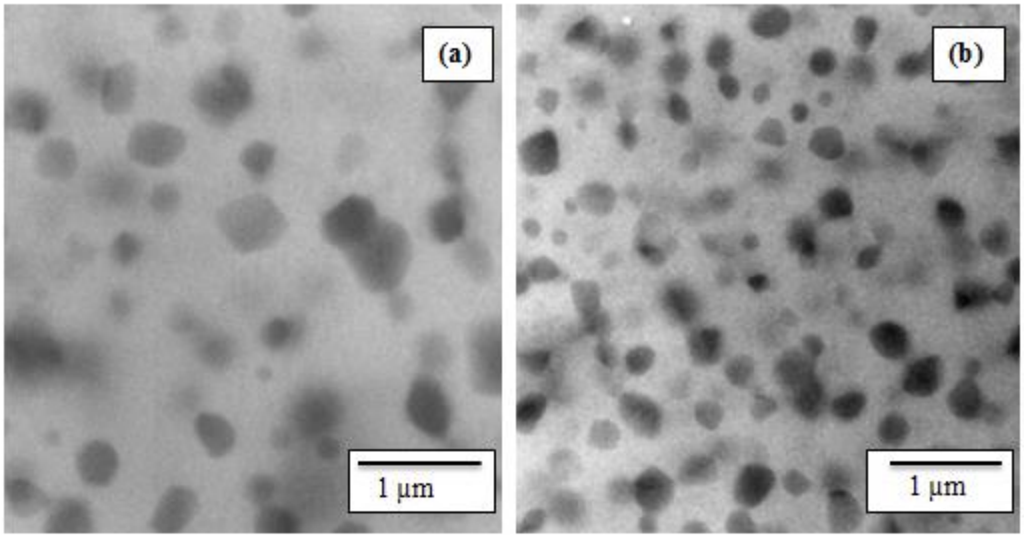

Figure 13 : Show the SEM images of the 70%Y-TZP/30% $MgAl_2O_4$ and 60% 3Y-TZP/40% $MgAl_2O_4$ nanocomposite sintered at 1300 °C

Figure 14 shows the X-ray diffraction pattern of the sintered 70% 3Y-TZP/30% $MgAl_2O_4$ sample. Again the patterns could completely indexed to a tetragonal unit which belongs to P42/nmx space group corresponding to yttria stabilized zirconia, and cubic unit, which belongs to Fd-3m space group corresponding to the spinel structure. The X-ray diffraction pattern of the sintered 70% 3Y-TZP/30% $MgAl_2O_4$ sample indicates that there was no phase change after sintering. However, the width of the peaks of the sintered sample were well developed compared to the diffraction pattern of the 70% 3Y-TZP/30% $MgAl_2O_4$ calcined powder. This is an indication of grain growth that occurred during sintering. An average crystallite size of 31nm was calculated using the Debye-Scherer equation.

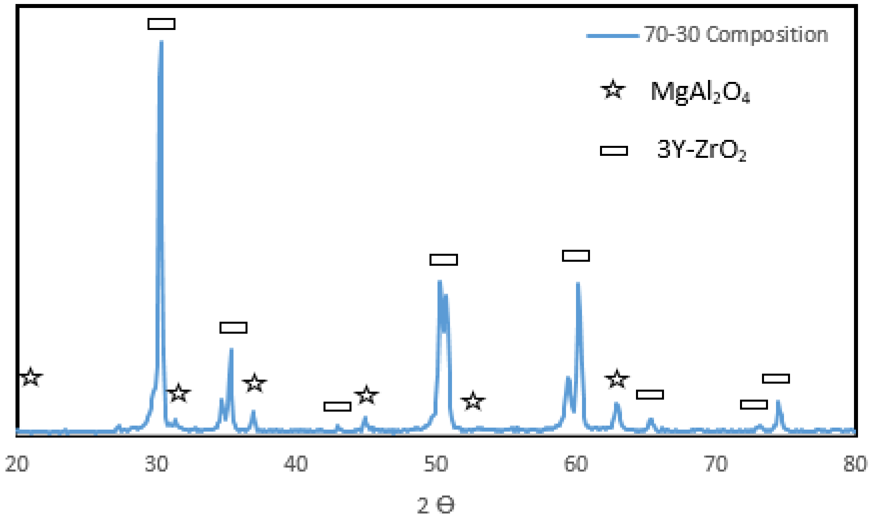

Figure 14 : X-ray diffraction pattern of the 70%3Y-TZP/30%$MgAl_2O_4$ nanocomposite sintered at 1300 °C and at zero minute dwell time.

Both the SEM and the X-ray diffraction pattern analysis of the sintered sample show slight but no significant grain growth. Suppression of grain growth during high temperature deformation is very important in obtaining high strain rate superplasticity. Grain growth increases the flow stress during high temperature superplastic deformation thereby limiting the tensile ductility and strain rates [2,12,18]. In the present study, the minimal grain growth observed in SEM and XRD analysis indicate that 3Y-TZP/$MgAl_2O_4$ nanocompsoties prepared by the coprecipitation techniques will exhibit high strain rate and enhanced tensile ductility due to the stability of grains at high temperature.

3.3: Density Measurements

The theoretical density of the 70%3Y-TZP/30%$MgAl_2O_4$ composite was previously calculated using by conventional rule of mixtures method. Density values of 5.31g/cm^3 [3] and 5.32 g/cm^3 [75] were recorded. In the present work, the theoretical density calculated using the same convectional rule of mixtures were 5.34g/cm^3 for 70%3Y-TZP/30% $MgAl_2O_4$ and 5.09g/cm^3 for the 60%3Y-TZP/40%$MgAl_2O_4$. The density of the sintered 70%3Y-TZP/30% $MgAl_2O_4$ and 60%3Y-TZP/40% $MgAl_2O_4$ powder compositions were calculated using the Archimedes equation in **4.3** below. All the measured densities at different sintering temperatures and sintering dwell times are given in the appendix A, B and C.

$$\text{Density} = \frac{\text{Dry Weight of Sample}}{\text{Dry Weight - Submerged Weight}} \times \text{Density of Water} \qquad (4.3)$$

The effect of sintering temperature and sintering dwell time on density were studied on both 70%3Y-TZP/30%$MgAl_2O_4$ and 60%3YTZP/40% $MgAl_2O_4$. **Figure 15** and **Table 4** show the results of the effect of sintering temperature evaluated on the 70%3YTZP/30% $MgAl_2O_4$ sintered samples. Regarding the effect of temperature, it is clearly seen from **Figure 15** that density rapidly increases from 1200 °C and reaches a maximum value of 1300 °C. Higher sintering temperatures resulted in a mild decrease in the density values possibly due to the fact that the applied pressure was kept constant at higher temperature. The SPS uses a combination of applied pressure and high heating rate to consolidate powders to full density. Therefore, increase in sintering temperature without corresponding increase in applied pressure impede densification mechanisms such as particle slidding and rearrangement.

The density of a material also plays an important role in the high temperature superplastic deformation in ceramics. In superplastic applications, ceramics with low densities may exhibit cavitation and subsequent premature failure in high temperature superplastic deformation. The combination of ball milling and the SPS synthesis technique used to synthesize the 70%3Y-TZP/30%$MgAl_2O_4$ nanocomposite yielded 98% [75] and 94% [3] theoretical density under similar sintering conditions employed in this research. In the present study, a dense nanocomposite with relative densities greater than 99.9% was obtained in both the 70%3Y-TZP/30%$MgAl_2O_4$ and 60%3Y-TZP/40%$MgAl_2O_4$ sintered samples at 1300 °C. These high densities at 1300 °C can be attributed to the combination of the coprecipitation synthesis technique which allowed the synthesis of smaller powder particles and the spark plasma sintering technique.

Table 4 : Density of 70%3Y-TZP/30%$MgAl_2O_4$ specimen at different sintering temperatures

Sintering Temperature (^OC)	Density (g/cm^3)	Relative Density (%)
1200	5.25	98.39
1300	5.34	99.96
1400	5.33	99.90
1500	5.28	98.83
1600	5.16	96.67

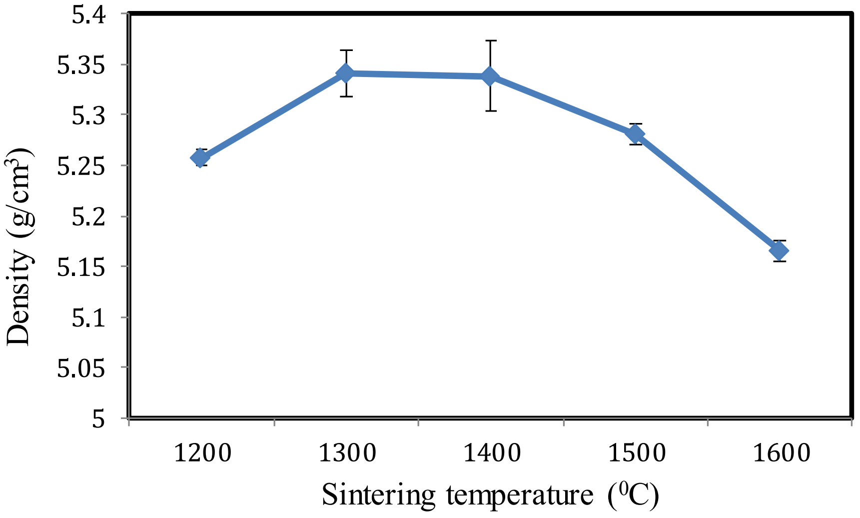

Figure 15 : Density as a function of sintering temperature of the 70%3Y-TZP/30%$MgAl_2O_4$ specimen sintered at zero min dwell time

Figure 16 shows the effect of sintering dwell time on density for both the 70%3Y-TZP/30%$MgAl_2O_4$ and 60%3Y-TZP/40%$MgAl_2O_4$ sintered samples. The densities for both compositions show a decrease in density with increasing sintering dwell time. Longer exposure of the sintered specimen to temperature causes an increase in grain growth, which in turn decreases the density. However, the decrease in density was very small. This was due to the high stability of the grains of 3Y-TZP/$MgAl_2O_4$ nanocomposite. In 3Y-TZP/$MgAl_2O_4$ nanocomposite, the $MgAl_2O_4$ phase, which has been proven to be superplastic [19], is introduced as a soft phase to supply Al^{3+} and Mg^{2+} to zirconia matrix [11,13,17]. These cations inhibit grain growth through particle pinning. In the present study, stability of 3Y-TZP/$MgAl_2O_4$ grains at high sintering temperature and longer sintering dwell time was due the presence of a spinel phase which supplied Mg^{2+} and Al^{3+} cations to suppress grain growth. The measured densities values with their corresponding sintering dwell time is shown in **Table 5** for the 70%3Y-TZP/30%$MgAl_2O_4$ and 60%3Y-TZP/40%$MgAl_2O_4$ nanocomposite.

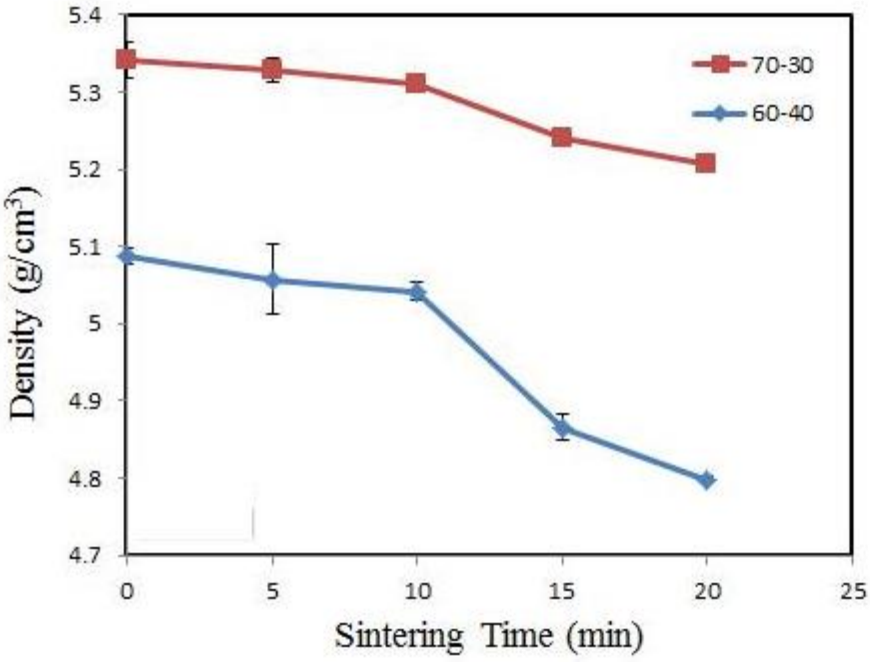

Figure 16 : Density as a function of sintering dwell time for 70%3Y-TZP/30%$MgAl_2O_4$ and 60%3Y-TZP/40%$MgAl_2O_4$ specimen sintered at 1300 °C

Table 5 : Density of 70%3Y-TZP/30%$MgAl_2O_4$ and 60%3Y-TZP/40%$MgAl_2O_4$ specimens at different sintering dwell time.

		70-30 Composition		60-40 Composition	
Time (min)	Temperature (°C)	Density (g/cm^3)	Relative Density (%)	Density (g/cm^3)	Relative Density (%)
0	1300	5.34	99.96	5.09	99.98
5	1300	5.33	99.72	5.06	99.39
10	1300	5.30	99.36	5.04	98.99
15	1300	5.24	98.05	4.95	97.23
20	1300	5.21	97.41	4.89	96.04

3.4: Mechanical Properties

Figure 17 illustrates the Vickers hardness of 70%3YTZP/30%$MgAl_2O_4$ and 60%3YTZP/40%$MgAl_2O_4$ nanocomposites as a function of sintering dwell time. The samples for the Vickers hardness experiment were sintered at 1300 °C because the highest density was obtained at that temperature. **Table 6** shows the effect of sintering dwell time on the 70%3YTZP/30%$MgAl_2O_4$ and 60%3YTZP/40%$MgAl_2O_4$ and their corresponding Vickers hardness The maximum Vickers hardness recorded was 15.3 GPa for 70%3YTZP/30%$MgAl_2O_4$ and 14.5 GPa for 60%3YTZP/40%$MgAl_2O_4$. Mahmood et al [3] used a combination of ball milling and spark plasma sintering technique under similar sintering conditions in the present study and obtained a Vickers hardness of 14 GPa in the 70%3YTZP/30%$MgAl_2O_4$ sintered nanocomposite. The difference in hardness values of their work and the present work clearly demonstrates the relationship between processing and mechanical properties. The synthesis technique used by Mahmood et al [3] to synthesized 70%3YTZP/30%$MgAl_2O_4$ resulted in an average grain size of ~ 100 nm after sintering. This reported average grain size is much bigger than the grain size obtained through the coprecipitation synthesis technique (31 nm). The smaller grain sizes increase the grain boundaries in 3Y-TZP/$MgAl_2O_4$ nanocomposite. These grain boundaries act as a barrier to dislocation motion, thereby increasing the hardness of the material.

Another observation from **Figure 17** is that the hardness values decrease with increasing sintering dwell time. The decrease in hardness value was due to grain growth, which occurs during sintering.

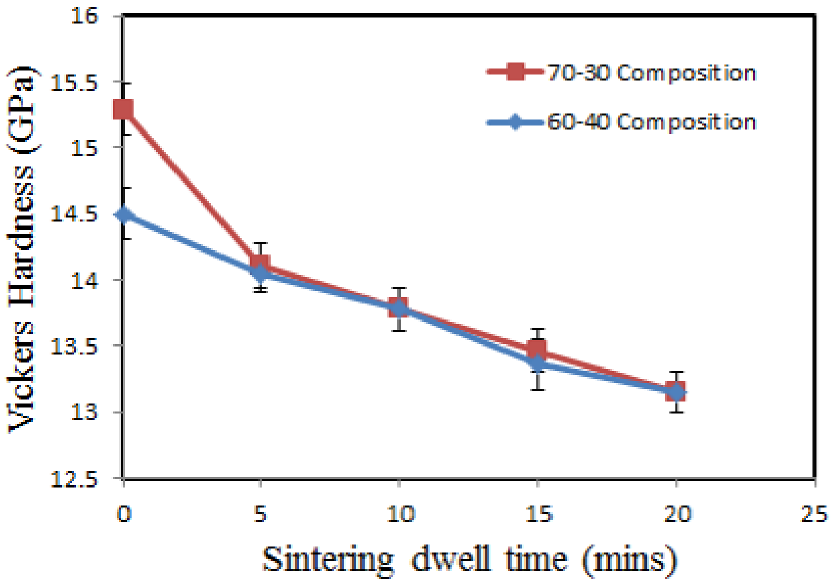

Figure 17 : Vickers hardness of the sintered 70%3Y-TZP/30%$MgAl_2O_4$ and 60%3Y-TZP/40% $MgAl_2O_4$ nanocomposite as a function of sintering dwell time.

Table 6 : The effect of sintering dwell time on the hardness of 70 %3Y-TZP/30%$MgAl_2O_4$ and 60%3Y-TZP/40%$MgAl_2O_4$ specimens.

		70-30 Composition	60-40 Composition
Sintering Dwell Time (min)	Sintering Temperature (°C)	Vickers Hardness (GPa)	Vickers Hardness (GPa)
0	1300	15.3	14.5
5	1300	14.3	14.1
10	1300	13.8	13.8
15	1300	13.5	13.4
20	1300	13.2	13.2

Figure 18 and **Table 7** show a variation of sintering temperature and the Vickers hardness of the 70%3Y-TZP/ 30%$MgAl_2O_4$ at zero minute dwell time. The Vickers hardness values increase to a maximum value at 1300 °C and then decreases slightly at higher temperatures due to grain growth. From this results, it is understood that the nano grains contained in both 70%3Y-TZP/ 30%$MgAl_2O_4$ nanocomposite are stable at high temperature and exhibited no significant grain growth.

Table 7 : Vickers hardness at different Sintering Temperature

Temperature (°C)	Vickerss Hardness (GPa)
1200	14.3
1300	15.3
1400	14.4
1500	14.2
1600	13.6

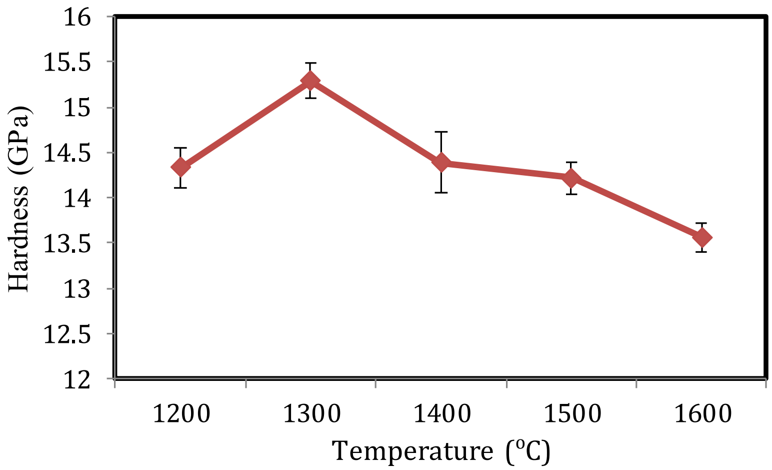

Figure 18 : Vickers Hardness of the sintered 70%3Y-TZP/30%$MgAl_2O_4$ nanocomposite as a function of sintering temperature

CHAPTER 4: CONCLUSIONS

The present work was undertaken to evaluate the potential of using the reverse coprecipitation technique to synthesize nanocomposite powders of 3Y-TZP/$MgAl_2O_4$ with microstructural features capable of exhibiting high strain rate superplasticity at low deformation temperature. Powders containing 70%3Y-TZP/30%$MgAl_2O_4$ and 60%3Y-TZP/40%$MgAl_2O_4$ were synthesized using the coprecipitation technique. A comparison of the microstructure of 3Y-TZP/$MgAl_2O_4$ produced by the coprecipitation was compared with the microstructure of 3Y-TZP/$MgAl_2O_4$ synthesized by the combination of ball mill and spark plasma sintering technique. The microstructures of the powders produced by the coprecipitation technique were investigated to determine the extent of particle agglomeration, crystallite size, elemental composition and particle size distribution of the powders. The microstructural evolution of 3Y-TZP/$MgAl_2O_4$ processed by the coprecipitation was found to be very different from the microstructure of 3YTZP/$MgAl_2O_4$ processed by a ball milling technique. The density and hardness of the 70% 3Y-TZP /30% $MgAl_2O_4$ and 60% 3Y-TZP/40% $MgAl_2O_4$ nanocomposites were also examined at different sintering temperature and sintering dwell time. The following are the key results of this study:

- SEM images of the 70%3Y-TZP/30%$MgAl_2O_4$ and 60%3Y-TZP/40%$MgAl_2O_4$ showed that the washing of the powders with an organic solvent reduced the extent of particle agglomeration.
- The X-ray diffraction patterns of both the 70%3Y-TZP/30%$MgAl_2O_4$ and 60%3Y-TZP/40%$MgAl_2O_4$ could be clearly indexed to tetragonal zirconia unit belonging to

the P42/nmx space group and cubic unit of spinel belonging to the Fd-3m space group.

- Crystallite size estimation from the X-ray diffraction patterns resulted in a crystallite size approximately 17nm for both the 70%3Y-TZP/30%$MgAl_2O_4$ and 60%3Y-TZP/40%$MgAl_2O_4$.
- The average particle size distribution of the TEM image of the 70%3Y-TZP/30%$MgAl_2O_4$ powder composition was 16 nm.
- STEM line scan confirms the elemental composition of 70%3Y-TZP/30%$MgAl_2O_4$ powder and the coexistence of two phases at the nano level.
- HRTEM image of the 70%3Y-TZP/30%$MgAl_2O_4$ calcined powder indicates the close proximity of the 3Y-TZP and $MgAl_2O_4$ phases at the nano level.
- The X-ray diffraction pattern of the sintered 70%3Y-TZP/30%$MgAl_2O_4$ indicates the phase are stable after sintering with no significant grain growth.
- The theoretical densities of the SPS sintered powders of 70%3Y-TZP/30%$MgAl_2O_4$ and 60%3Y-TZP/40%$MgAl_2O_4$ were 99.96% and 99.98% respectively.
- The Vickers hardness of the 70%3Y-TZP/30%$MgAl_2O_4$ and 60%3Y-TZP/40%$MgAl_2O_4$ recorded were 15.7 GPa and 14.5 GPa respectively.

REFERENCES

1. F. Wakai, N. Kondo, Y. Shinoda, “Ceramics Superplasticity,” *Current Opinion in Solid State and Materials Science*, **4**, 461- 465 (1999).
2. B-N. Kim, K. Hiraga, “Superplastic Ceramic Deformation at High Strain Rates,” *Chemical Engineering Technology*, **25** [10], 1021-1023 (2002).
3. M. Shirooyeh, S. Tanju, J. E. Garay, T. G. Langdon, “Characterization of Potential Superplastic Zirconia-Spinel Nanocomposite Processed by Spark Plasma Sintering,” *Ceramic Engineering and Science Proceedings*, **30** [8], 31-36 (2010).
4. T. G. Langdon, “Seventy-Five Years of Superplasticity: Historic Development and New Opportunities,” *Journal of Materials Science*, **44**, 5998-6010 (2009).
5. G. D. Zhan, J. E. Garay, A. K. Mukherjee, “Ultralow-Temperature Superplasticity in Nanoceramics Composites,” *Nano Letters*, **5** [12], 2593-2597 (2005).
6. F. Wakai, S. Sakagughi, Y. Matsuno, “Superplasticity of Yttria-Stabilized Tetragonal ZrO_2 Polycrystal,” *Advanced Ceramic Materials*, **1**, 259-263 (1986).
7. B-N. Kim, K. Hiraga, K. Morita, Y. Sakka “A High-Strain Superplastic Ceramic,” *Nature*, **413**, 288-290 (2001).
8. A. Dominguez-Rodriguez, M. Jimenez-Melendo, “Superplasticity of YTZP: New Approach and Application,” *Materials Transactions*, JIM, **40**, NO. 8, 830-835 (1999).
9. T. Sakuma, Y. Yoshizawa, K. Kajihara, “Superplasticity in Tetragonal Zirconia Polycrystal,” *Annales de chimie Science des mate’riaux*, **18** [5-6], 361-67 (1993).
10. T. G. Nieh, J. Wadsworth, “Superplastic Ceramics,” *Annual Review Material Science*, **20**, 117-140 (1990).

11. K. Morita, K. Hiraga, B.-N. Kim, Y. Sakka, “Effect of $MgAl_2O_4$ Spinel Dispersion on High-Strain-Rate Superplasticity in Tetragonal ZrO_2 Polycrystal,” *Materials Transactions*, **45** [7], 2073-2077 (2004).
12. K. Hiraga, B-N. Kim, K. Morita, H. Yoshida, T. S. Suzuki, Y. Sakka, “High-Strain Rate Superplasticity in Oxide Ceramics,” *Science and Technology of Advanced Materials*, **8**, 578-587 (2007).
13. K. Morita, B-N. Kim, H. Yoshida, Y. Sakka, K. Hiraga, “Development of High-Strain Rate Superplastic Oxide Ceramics Based on Flow Mechanism,” *Materials Science Forum*, **735**, 9-14 (2013).
14. H. Yoshida, K. Matsui, Y. Ikuhara, “Low-Temperature Superplasticity in Nanocrystalline Tetragonal Zirconia Polycrystal (TZP),” *Journal of the American Ceramic Society*, **95** [5], 1701-1708 (2012).
15. I-Wei Chen, L. An Xue, “Development of Superplastic Ceramics, *Journal of the American Ceramic Society*, **73**[9], 2585-2609 (1990).
16. K. Morita, K. Hiraga, B-N. Kim, H. Yoshida, Y. Sakka, “Fabrication of Nanocrystalline Superplastic ZrO_2 Ceramics, *Materials Science Forum*, **551-552**, 491-496 (2007).
17. K. Morita, K. Hiraga, Y. Sakka, “High-Strain Rate Superplasticity in Y_2O_3-Stabilized Tetragonal ZrO_2 Dispersed with 30 vol% $MgAl_2O_4$ Spinel,” *Journal of the American Ceramic Society*, **85** [7],1900-1902 (2002).
18. K. Hiraga, B-N. Kim, K. Morita, Y. Sakka, “High-Strain Rate Superplasticity in Oxide Ceramics,” *Materials Science Forum*, **447-448**, 291-298 (2004).

19. M. Oka, N. Tabuchi, T. Takashi, "High-Strain Rate Superplasticity in Ceramics," *Materials Science Forum*, **304-306**, 451-458 (1999).
20. F. Wakai, A. Domínguez-Rodríguez, "Grain Boundary Dynamics in Ceramic Superplasticity," *Nanomaterials From Research To Applications*, Edited by H. Hoson, Y. Mishima, H. Takezoe, K. J. D. Mackenzie, Elsevier Ltd, Great Britain, 297-310 (2006).
21. E. H. Kisi, C. J. Howard, "Crystal Structures of Zirconia Phases and their Inter-Relation," *Engineering Materials*, **153-154**, 1-36 (1998).
22. I. Nettleship, R. Stevens, "Tetragonal Zirconia Polycrystal (TZP) - Review," *International Journal of High Technology Ceramics*, **3** [1], 1-32 (1987).
23. M. Yoshimura, "Phase Stability of Zirconia," *Journal of the American Ceramic Society*, **67** [12], 1950-1955, (1988).
24. J. Swab, "Role of Oxide Additives in Stabilizing Zirconia for Coating Applications", *Weapon and Materials Research Directorate*, ARL-TR-2591 (2001).
25. K. Matsui, H. Yoshida, Y. Ikuhara, "Grain-Boundary Structure and Microstructure Development Mechanism in 2-8 mol% Yttria-Stablized Zirconia Polycrystals," *Acta Materialia*, **56**, 1315-1325 (2008).
26. O .A. Graeve, "Zirconia," *Ceramics and Glass Materials, Structure, Properties and Processing*, Edited by J. F. Shockelford, R.H. Doremus, Springer, New York, ISBN 978-0-387-73361-6 (2008).
27. F. Maglia, I. G. Tredici, U. Anselmi-Tamburini, "Densification and Properties of Bulk Nanocrystallization Functional Ceramics with Grain Size below 50 nm," *Journal of the European Ceramic Society*, **33**, 1045-1066 (2013).

28. A. Suresh, M. J. Mayo, W. D. Poter and C.J. Rawn "Crystallite and Grain-Size-Dependent Phase Transformations in Yttria-Doped Zirconia," *Journal of the American Ceramic Society*, **86** [2], 360-362 (2003).
29. T. Chraska, A. H. King, C. C. Berndt, "On the Size-Dependent Phase Transformation in Nanoparticle/Zirconia," *Materials Science and Engineering A*, **286**, 169-178 (2000).
30. K. C. Patil, M. S. Hedge, T. Rattan, S. T. Aruna, "Chemistry of Nanocrystalline Oxide Materials, Combustion Synthesis, Properties and Applications," *Word Scientific*, 210-214 (2008).
31. H. G. Scott, "Phase Relationships in the Zirconia-Yttria System," *Journal of Materials Science*," **10**, 1572-1535 (1975).
32. T. S. Suzuki, Y. Sakka, K. Morita, K. Hariga, "Enhanced Superplasticity in a Alumina-Containing Zirconia Prepared by Colloidal Processing," *Scripta Materialia*, **42**, 705-710 (2000).
33. Y. Sakka, T. Ishii, T. S. Suzuki, K. Morita, K. Hiraga, "Fabrication of High-Strain Rate Superplastic Yttria-Doped Zirconia Polycrystal by Adding Manganese and Aluminum Oxides," *Journal of the European Ceramic Society*, **24**, 449-453 (2004).
34. K. Kajihara, Y. Yoshizawa, T. Sakuma, "The Enhancement of Superplastic Flow in Tetragonal Zirconia Polycrystal with SiO_2-Doping*," Acta Meta Material*, **43** No.3, 1235-1242 (1995).

35. R. Wananuruksawong, Y. Shinoda, T. Akatsu, Fumihiro Wakai, "Evolution of Microstructure and Intergranular Glass Chemistry in Plastically Deformed Nanocrystalline Si_3N_4 Ceramics," *Journal of the American Ceramic Society,* 1-8 (2014). DOI: 10.1111/jace.13259.

36. M. Mitomo, H. Hirotsutru, H. Suematsu, T. Nishimura, "Fine-Grained Silicon Nitride Ceramics Prepared from β-Powder," *Journal of the American Ceramic Society*, **78**, 211-214 (1995).

37. J. A. Schneider, A. K. Mukherjee "Effect of Microstructure on the Deformation Mechanism in Silicon Nitride," *Journal of the American Ceramic Society*, **82**, 761-764 (1999).

38. F. Wakai, Y. Kodama, S. Sakaguchi, N. Murayama, K. Izaki, K. Niihara, "A superplastic Covalent Crystal Composite," *Nature*, **344**, 421- 423 (1990).

39. X. Wu, I-W. Chen, "Exaggerated Texture and Grain Growth in a Superplastic SiAlON," *Journal of the American Ceramic Society*, **75** [10], 2733-2741 (1992).

40. S-L. Hwang, I-W. Chen, "Superplastic Forming of SiAlON Ceramics," *Journal of the American Ceramic Society*, **77** [10], 2575-2585 (1994).

41. J. J. Melendez-Martinez, "Creep of Silicon Nitride," *Progress in Materials Science*, **49**, 19-107 (2004).

42. A. Rosenflanz, I-W. Chen, "Classical Superplasticity of SiAlON Ceramics," *Journal of the American Ceramic Society*, **80**, 1341-1352 (1997).

43. L. A. Xue, Xin Wu, I-W. Chen, "Superplastic Alumina Ceramics with Grain Growth Inhibitors," *Journal of the American Ceramic Society*, **74** [4], 842-45 (1999).

44. Y. Yoshizawa, T. Sakuma, "Improvement of Tensile Ductility in High-Purity Alumina Due to Magnesia Addition," *Acta Metall.Mater.*, **40** NO.11, 2943-2950 (1992).
45. L. A. Xue, I-W. Chen, "Superplastic Alumina at Temperatures below 1300 ℃ Using Charge – Compensating Dopant," *Journal of the American Ceramic Society*, **79** [1], 233-238 (1996).
46. Y. Takigawa, Y. Yoshizawa, T. Sakuma, "Superplasticity in Al_2O_3-20Vol% Spinel (MgO.1.5Al_2O_3) Ceramic," *Ceramic International*, **24**, 61- 66 (1998).
47. K. A. Hing, P. A. Ravell, N. Smith, T. Buckland, "Effect of Silicon Level on Rate, Quality and Progression of Bone Healing within Silicate - Substituted Porous Hydroxyapatite Scaffolds," *Biomaterials*, **27**, 5014-5026 (2006).
48. K. Tago, K. Itatani, T. S. Suzuki, Y. Sakka, Seiichiro Koda, "Densification and Superplasticity of Hydroxyapatite Ceramics," *Journal of the Ceramics Society of Japan*, **113** [10], 669-673 (2005).
49. H. Yoshida, B-N. Kim, H-W. Son, Y-H. Han and S. Kim, "Superplastic Deformation of Transparent Hydroxyapatite," *Scripta Materialia*, **69**, 155-158 (2013).
50. W. J. Kim, J. Wolfenstine, G. Frommeyer, O. A. Ruano, O. D. Sherby, " Superplastic Behavior of Carbide," *Scripta, Metallurgica*, **23**,1515-1520 (1989).
51. P. M. Ajayan, "Bulk Metal and Ceramic Nanocomposites," *Nanocomposite Science and Technology*, Edited by P.M. Ajayan, L. S. Schadler, P.V. Braun, WILEY- VCH Verlag GmbH & Co. KGaA, Weinheim, 3-527-3059-6, (2003).
52. P. H. C. Camargo, K. G. Satyanarayana, F. Wypych, "Nanocomposites: Synthesis, Structure, Properties and New Application Opportunities," *Materials Research*, **12** NO. 1, 1-39 (2009).

53. C. Suryanarayana, "Synthesis of Nanocomposites by Mechanical Alloying," *Journal of Alloys and Compounds*, **509 S**, S229 – S234 (2011).
54. G-M. Chow, L. K. Kurihara, "Chemical Synthesis and Processing of Nanostructructrued Powders and Films," *Nanostructured Materials, Processing, Properties and Potential Applications*, Edited by Carl C. Koch, Noyes Publications / William Andrew Publishing, New York, 0-8155-1451-4, 3-39 (2002).
55. H. J. Fecht, "Nanostructured Materials and Composites Prepared by Solid State Processing," Nanostructured Materials, *Processing, Properties and Potential Applications*" Edited by Carl C. Koch, Noyes Publications/William Andrew Publishing, New York, 0-8155-1451-4, 73-107 (2002).
56. C. Suryanarayana, E. Ivanov, V. V. Boldyrev, "The Science and Technology of Mechanical Alloying," *Materials Science and Engineering A*, **304-306**, 151-158 (2001).
57. C. Suryanarayana, "Mechanical Alloying and Milling," *Progress in Materials Science*, **46**, 1-184 (2001).
58. B. S. Murty, S. Ranganathan, "Novel Materials Synthesis by Mechanical Alloying/Milling," *International Materials Reviews*, **43** No.3, 101-141 (1998).
59. F. Karimzadeh, M.H. Enayati, M. Tavoosi, "Synthesis and Characterization of Zn/Al_2O_3 Nanocomposite by Mechanical Alloying," *Materials science A*, **486**, 45-48 (2008).
60. G. Skandan, A. Singhal, "Perspectives on the Science and Technology of Nanoparticle Synthesis," *Nanomaterials Handbook* , Edited by Yury Gogotsi, CRC Taylor & Francis, New York, 0-8493-208-8,13-26 (2006).

61. M. J. Readey, R-R. Lee, J. W. Halloran, A. HL Heurer, " Processing and Sintering of Ultrafine MgO-ZrO_2 and ($MgO_2Y_2O_3$)-ZrO_2 Powders," *Journal of The American ceramic Society*, **73**[6], 1499-1503 (1990).
62. Z. Pedzich, K. Haberko, "Coprecipitation Conditions and Compaction Behavior of Y-TZP Nanomeric Powders," *Ceramic International*, **20**, 85-89 (1994).
63. M. J. Mayo, D. C. Hague, D-J. Chen, "Processing Nanocrystalline Ceramics for Applications in Superplasticity," *Materials Science and Engineering A*, **166**, 145-159 (1993).
64. M. J. Readey and D. W. Readey, "Sintering of ZrO_2 in HCl Atmosphere, "*Journal of The American Ceramic Society*, **69** [7], 580-582 (1986).
65. H. P. Li, "Effect of Hydroxide Gel Drying the Characteristics of Coprecipitated Zirconia-Hafnia Powders," *Journal of Materials Science*, **28** [2], 553-560 (1993).
66. M. Kaliszewski "Alcohol interaction with zirconia," *Journal of the American Ceramic Society*, **73** [6], 1504-1509 (1990).
67. G. Glaspell, V. Abdelsayed, K. M. Saoud, M. Samy El-Shall, "Vapor-phase synthesis of metallic and intermetallic nanoparticle and nanowires Magnetic and catalytic properties," *Pure Applied Chemistry*, **78** No. 9, 1667-1689 (2006).
68. M. T. Swihart, "Vapor-phase synthesis of nanoparticle," *Current Opinion in Colloid and Interface Science*, **8**, 127-13 (2003).
69. T. Yamamoto, R. D. Shull, P. R. Bandaru, F. Cosandey, " Superparamagnetic Nanocomposites of Silver/Iron oxide by inert gas condensation, *Japan Journal of Applied Physics* , **33** ,1301- 1303 (1994).

70. ASTM International Designation: E384-10$^{\varepsilon2}$, Standard Test Method for Knoop and Vickers Hardness of Materials, 2-10 (2010).

71. B. D. Cullity, "Elements of X-ray Diffraction,"Addison-Wesley Publishing Company, Inc., Reading, Massachusetts, 78-99 (1956).

72. R. A. Kimel, "Yttria-Tetragonal Stabilized Zirconia Aqueous Synthesis and Processing," *Dekker Encyclopedia of Nanoscience and Nanotechnology*, Marcel Dekker, New York, 3973-3976 (2004).

73. K. Morita, K. Hiraga, B.-N. Kim, H. Yoshida, Y. Sakka, " Synthesis of Dense Nanocrystallined ZrO_2-$MgAl_2O_4$ Spinel Composite," *Scripta Materialia*, 53,1007-1012 (2005).

APPENDIX A: Density measurements of the 70%3Y-TZP/ 30%$MgAl_2O_4$ at different sintering temperatures

Sintering Temperature (°C)	1200	1300	1400	1500	1600
Sample 1	5.25774 5.25774 5.24546	5.35117 5.33178 5.32734	5.30855 5.28889 5.32734	5.28911 5.29502 5.28066	5.16002 5.16002 5.18440
Sample 2	5.27009 5.25774 5.25774	5.36505 5.36459 5.30848	5.37014 5.36354 5.37014	5.27257 5.27955 5.26893	5.16002 5.16752 5.16002
Average Density (g/cm^3)	**5.25775**	**5.34140**	**5.33810**	**5.28097**	**5.16533**

APPENDIX B: Density measurements of the 70%3Y-TZP/ 30%$MgAl_2O_4$ at different sintering dwell times.

Sintering Dwell Time (minute)	0	5	10	15	20
Sample 1	5.351176 5.331785 5.327340	5.34511 5.34511 5.32960	5.31457 5.30055 5.31457	5.24764 5.23634 5.24764	5.21530 5.20479 5.19632
Sample 2	5.365052 5.364590 5.308481	5.30661 5.31127 5.33152	5.30983 5.30983 5.30675	5.22245 5.23368 5.24764	5.21530 5.19632 5.20479
Average Density (g/cm^3)	**5.34140**	**5.32820**	**5.30935**	**5.23923**	**5.20547**

APPENDIX C: Density measurements of the 60%3Y-TZP/40%$MgAl_2O_4$ at different sintering temperatures.

Sintering Dwell Time (min)	0	5	10	15	20
Sample 1	5.08472 5.07591 5.07945	5.097987 5.097987 5.078275	5.05533 5.05533 5.03500	4.96822 4.98341 4.95615	4.88907 4.88190 4.88589
Sample 2	5.08931 5.08755 5.08931	5.016042 5.014707 5.016042	5.04175 5.03500 5.02826	4.93472 4.92625 4.94902	4.88671 4.88507 4.88907
Average Density (g/cm^3)	**5.08437**	**5.05350**	**5.04178**	**4.95296**	**4.88628**